





Research Article

Numerical Simulation of the Effect of Fusion Welding Processes on Residual Stress in Stainless Steel Pipe Weld Joints Used in Fast Reactors

M Ragavendran^{1,2*} , M Vasudevan^{1,2} 

¹Homi Bhabha National Institute, Indira Gandhi Centre for Atomic Research, Kalpakkam, Tamil Nadu, India

²Materials Development and Technology Division, Metallurgy and Materials Group, Indira Gandhi Centre for Atomic Research, Kalpakkam, Tamil Nadu, India

Email: mragavendran93@gmail.com

Received: 1 July 2023; **Revised:** 9 September 2023; **Accepted:** 7 November 2023

Abstract: The main structural material used in the building of Fast Breeder Reactors (FBR) is stainless steel of type 316L(N). Finite Element Model (FEM)-based simulations were carried out to understand the effect of various welding processes on the residual stresses induced in 316L(N) stainless steel primary sodium-carrying pipes with an inner diameter of 208 mm and a wall thickness of 5.6 mm. The welding processes considered include multi-pass Tungsten Inert Gas (TIG) welding, A-TIG, laser, hybrid laser-TIG, and Hybrid laser-Metal Inert Gas (MIG). First, single or hybrid heat sources are chosen based on the welding process, and then weld bead profiles obtained during simulation are made to match with that of the actual weld bead profiles obtained during experiments. Then, the optimised heat source is employed for the thermal analysis. The thermal analysis output is then successively linked and provided as input to the mechanical analysis, which uses an isotropic hardening model to predict hoop and axial residual stresses in pipe weld joints. The results show that the A-TIG weld joint exhibited lower hoop stress (165 MPa at inner diameter and -2 MPa at outer diameter) in comparison with that of the other weld joints. The lower residual stress is attributed due to the straight-sided weld bead, lower peak temperature, and slower cooling rate of the A-TIG welding. Therefore, A-TIG welding is recommended among the chosen fusion welding processes for welding of 316L(N) stainless steel primary sodium carrying pipes to minimise the residual stresses and mitigate the premature failure of the pipe weld joints.

Keywords: numerical simulation, fusion welding, residual stress, stainless steel, pipe welding

1. Introduction

The type of heat source and consumables utilised are the main factors used to categorise welding operations. Fusion welding procedures fall into two categories: arc-based processes and beam-based processes, depending on the heat source. In the past, engineering components were most frequently manufactured using arc welding procedures. The main advantage of arc welding is its minimal initial investment. However, it has some drawbacks, including a high heat input, groove preparation, and numerous passes for thicker materials. As a result, productivity is decreased, and welded components are more likely to distort. In the engineering sector, laser welding is used to overcome the drawbacks of

arc-based welding procedures. The laser can be concentrated in a very small area, resulting in a higher power density and higher penetration, which will help to reduce the need for multiple passes. In addition, compared with arc welding procedures, the heat input associated with laser welding is smaller. The weld metal volume will be reduced, and the narrower the Heat-Affected Zone (HAZ), the lesser the residual stress and deformation will be. However, there are certain disadvantages to laser welding as well, such as costly capital expenditure, tightly fitting weldable components, hot cracking, and porosity issues.

Arc and laser welding are combined to create a single weld pool by hybrid welding in order to overcome their drawbacks and reap their benefits. High melting efficiency, wide gap-bridging ranges, and high productivity are the key benefits. TIG or MIG can be used as the arc welding source. The depth of penetration will increase by more than 250 percent when the low-power laser welding equipment is connected to the available arc heat source.

Bouchard has investigated many variables that impact the intensity and range of residual stresses and deformation in welded components. Its engineering performance is impacted by the welding process (heat input, number of passes), weld geometry (including the impact of structural restraint), weld and base material properties, as well as microstructural alterations and related transformation plasticity [1]. The Heat-Affected Zone (HAZ) of the weld metal contains the welding residual stress peak values. As the welding heat input reduces, the residual stress value also decreases [2]. Chen et al. utilised a thermometallurgical-mechanical model and looked into how groove type affected welding residual stress and deformation at weld sites. The findings demonstrate that the groove type significantly affects the temperature history, residual stress distribution, and simulated deformation [3].

Therefore, it is preferable to measure or anticipate the amount of residual stress and deformation generated by the various welding procedures prior to bringing it into service.

To measure and estimate the degree of deformation in the components, simulation and numerical modelling of the welding process are useful tools. At any location in the structure, it provides and quantifies the evolution of stress, strain, and temperature. Wen et al. used ideal welding process parameters to minimise the welding-induced deformations after analysing the submerged arc welding process [4]. Thus, FEM is a useful tool for process development and can be used to better understand the welding process. Jiang et al. employed heat sink technology to lower the residual stress in type 316L stainless steel joints caused by an increase in the average heat transfer coefficient. They verified the created model and discovered a twenty percent decrease in the maximum tensile longitudinal stress in weld joints [5]. The Hybrid Laser-MIG (HLM) weld joint's narrower weld bead geometry showed a much narrower tensile stress distribution than the arc-based hot wire TIG weld joint [6]. The computational results demonstrate that the welding residual stress distribution is highly influenced by the weld metal volume and that the residual stress prediction accuracy depends on hardening models [7]. Using three-dimensional finite element analysis, temperature, and residual stress distributions in SS304 materials for the nuclear industry are successfully studied using ANSYS. Transverse analysis of residual stress provides insight into structural stability [8]. Residual stresses caused by weld repair on weld joints made of austenitic stainless steel are increased by more than 100 percent. The stresses assessed by the Finite Element (FE) analysis are consistent with the experimental pattern [9]. The FEM model supports the practicality of overlay welding for pressure pipe repair welding, which may result in compressive residual stress within the weld seam [10]. A weld overlay effectively prevents crack propagation in subsequent operations by applying compressive loads to the pipe's inner surface [11]. The nature of residual stress and its distribution depend on the type of material, heat source, number of thermal cycles, geometry, constraints, type of welding process, heat treatment procedure, and various other factors. The relationship between the peak tensile residual in the welded components and the material yield strength was proportional [12].

Miyasaka et al. has developed a simulation model to simulate the welding of a pipe and plate and found that the geometry of the workpiece significantly affects heat flow. The shape of a modelling workpiece must be as similar to the real one as possible for a modelling simulation to be effective [13]. Using the restraint factor, a highly effective computational approach for modelling welding residual stress might be created for materials used in nuclear reactors [14].

Duranton et al. proved that the 3D model produces a more accurate and realistic stress calculation than the 2D model by analysing the FEM of multipass welding type 316L stainless steel pipe with an adaptive mesh methodology [15]. Xu et al. performed a pipe welding simulation for axisymmetric 2D models and 3D pipes in order to determine the residual stress. The 3D model results showed that the welding pool's maximum temperature ascended along the entire welding line throughout the welding process, and that the welding pool's width and depth likewise increased as the

heat source moved. In addition, the residual stress values for the 3D model are greater than those for the axisymmetric 2D model [16]. The residual stress of an arc-welded austenitic pipe was predicted using an ensemble of artificial neural networks utilising experimental data, and the results demonstrate that the predictions for the axial and hoop residual stresses were significantly closer to the experimental measurements [17]. The maximum values of the tensile and compressive residual stresses will decrease when longer sleeves are employed for in-service welding of pipelines, according to FE modelling of the effect of sleeve length on residual stress [18].

Deng and Murakawa modelled the thermal history and residual stress in multi-pass welds on stainless steel pipes. They observed that the welding residual stress patterns and temperature cycles predicted by the 3D FE model corresponded extremely well with the experimental observations [19]. The welding residual stress is significantly influenced by the weld metal yield strength. Findings from Kermanpur et al. showed that for the welding of thin-walled pipes, a volumetric arc heat input best matched the thermocouple data. Additionally, it was demonstrated that increasing the heat input caused the heat-affected zone's peak temperature to increase and the weld pool root to spread out, which was in accordance with the findings [20]. Kiyoshima et al. examined how a heat source model affected the welding of residual stress and distortion in a multi-pass J-groove weld. The numerical results demonstrate that heat source models have an impact on the distribution and distortions of the welding residual stress. When prediction accuracy and computation time are balanced, it is observed that the strategy based on variable-length heat sources may predict a reasonable result for residual stress while reducing a significant amount of time on numerical analysis [21]. When residual stress in a 316L electron beam weld joint was predicted using plastic parameters obtained from a crystal plasticity finite element model, excellent agreement was seen between the results and the residual strain data from X-ray diffraction [22]. The simulation findings demonstrate that the sample without flux has a higher maximum temperature. It is relevant to the evaluation of welding-induced residual stress and distortion in A-TIG welding of duplex stainless steel [23]. The internal and surface residual stresses of the thick plates are symmetrical along the paths perpendicular to the weld seam, with asymmetry occurring in the weld seam and the heat-affected zone where the stress varies [24]. The double-side welding techniques used resulted in residual axial and hoop stresses that were tensile at the inner and outer surfaces of the dissimilar weld joint [25].

A 3D FEM model predicted a strong stress peak near the weld start point, approximately 74% of the material's yield strength, and a non-uniform residual stress distribution in the circumferential and through-thickness directions [26]. Through-wall bending dominates the residual stress distribution in thin-walled pipes with few passes and is caused by the tourniquet contraction of the whole weld line. A cosinusoidal distribution of stress, caused by the deformations created around individual passes, is superimposed on any through-wall bending as the thickness and number of weld passes increase [27]. The base metal variation significantly influences the axial stress fluctuations in the inner and outer surfaces. The number of passes has a less significant impact on residual stresses than on pipe material type, particularly on the outer surface of the same thickness. For the SUS304 pipe, preheating at least 325 °C is necessary to maintain the tensile axial residual stress below the base metal yield strength [28].

The welding speed and heat input significantly impact the hoop stresses more than the axial stresses. In addition, compared to a two-pass welding method, a three-pass welding procedure produces substantially lower stress [29]. It has been discovered that the effect of external restriction works primarily in the cooling process by increasing tensile plastic strain to lower the shrinkage force in both the axial and hoop directions. As a result, the welding deformation and residual stresses are noticeably reduced [30].

Deng and Kiyoshima performed a laser welding simulation of residual stresses in a stainless steel pipe while accounting for the influence of the initial residual stress. The numerical results show that the initial residual stresses before welding significantly affect the residual stresses after welding in the pipe model [31]. Arif et al. carried out a thermal analysis of a spiral laser-welded tube and showed that the high-stress zone narrowed as welding speed was increased at consistent power [32]. Xu et al. compared residual stress produced by TIG and Laser Beam Welding (LBW) in welds of AISI 304 stainless steel pipes via numerical modelling and validation. Considering residual stress, deformation, and production efficiency, the results indicated that the LBW is preferable to the TIG for welding AISI 304 stainless steel pipes [33]. When using advanced welding processes with low welding passes and which have seen low thermal cycles, the tensile residual stress behaviour was 25% less evident than when using conventional welding, which exhibits high tensile behaviour in the hoop direction up to a depth of more than 50% of the thickness [34].

Kong et al. developed a Finite Element Model (FEM) to investigate residual stress in hybrid laser-Gas Metal

Arc (GMA) welding. The findings suggest that higher welding speed might effectively lower the residual stress concentration. The created model might enhance the operational parameters for hybrid laser-GMA welding and other welding methods [35]. A thermodynamic study of multi-pass TIG and A-TIG welding of 2.25 Cr-1Mo steel was carried out by Pavan et al. They found that the distortion in the multi-pass TIG weld joint was more pronounced because it required more weld passes to fill the V-groove, which increased the volume of the weld metal. The thermomechanical analysis utilised in the comparison study showed that employing the A-TIG welding process will significantly reduce the degree of distortion [36]. The welding start point of circumferential welds determines the welding-induced plastic deformation and residual stress [37]. The development of potentially dangerous tensile stress creation at existing weld root toes, which can be detrimental to Stress Corrosion Cracking (SCC) and reheat cracking in ageing welds of power and process piping structures, can be seen in the residual stress distribution on pipe inner surfaces between neighbouring weld root toes [38]. The HAZ of the circumferential weld's resistance to SCC is reduced by coarse grains. The principal factor causing SCC is the high axial stress component produced by the welding residual stress and working loads [39]. The welding highly sequences influence the induced residual stresses and distortions in intensity and distribution. Full circumferential welding on both the inner and outer surfaces shows the most consistent distribution of axial residual stress [40]. The uphill side is crucial as residual stresses increase with the tube's inclination degree. Residual stress decreases with the thickness of the tubes. Axial and hoop residual stresses tend to increase when the yield strength of a material increase [41]. The welding process significantly impacts the residual stress on the pipe's inner wall, whereas the residual stress on the pipe's outer wall is less affected. Although the residual stress level can be altered, the distribution of the residual stress cannot be modified by changing the welding sequence [42].

Yaghi et al. performed a numerical simulation to examine the effects of wall thickness and bead count on residual stresses in stainless steel welded pipes. The results demonstrate that pipe diameter significantly affects residual axial and hoop stresses at the outer side in thick-walled FE models but has no effect on axial and hoop stresses at the inner side in thin-walled FE models [43]. Deng and Kiyoshima computed residual stresses in a girth-welded pipe, highlighting the focus of stress at the start/end of the weld. The findings reveal substantial gradients in the hoop and axial residual stresses at the weld start/completion area, which differ noticeably from those in the steady range [44]. Liu et al. examined the development and concentration of residual stress in multipass narrow-gap welds on thick-walled stainless steel pipes. The results show that the weld's through-wall hoop residual stress is primarily tensile. Maximum tensile stresses and changes in the axial and hoop stress distributions are almost identical when the groove is finished to a particular height [45].

Austenitic stainless steel of type 316L(N) is an important structural and piping material in fast reactors. The literature on numerical modelling of residual stress caused by various welding methods, including the beam type that is being considered for use in the manufacturing of sodium transporting pipes, is scarce. Traditional TIG, A-TIG, and cutting-edge welding procedures, including laser, hybrid laser-TIG, and hybrid laser-MIG processes, are all considered in this work. In order to predict the axial and hoop residual stresses in 316L(N) stainless steel pipe weld joints, which are employed as the major sodium transportation pipes in fast reactors, this work discusses numerical modelling. Depending on the welding process, single and hybrid heat sources have been employed to precisely predict the residual stresses.

2. Finite element analysis

In general, welding modelling consists of a structural analysis made from the thermal output, followed by a thermal analysis that shows the thermal process during welding and culminates by exhibiting the temperature gradients related to welding. The mechanical analysis uses the results of the thermal analysis, such as the thermal history, as input. The residual stress, stresses, and deformation in the welded component are the outcomes of the mechanical study. In this paper, the sequential coupling technique is used for this type of analysis. The impact of welding processes is described in this paper using a numerical simulation method that relies on thermal elastic-plastic FEM and related heat source models on final residual stresses after welding in an austenitic stainless steel model pipe using SYSWELD® software, which is used to do realistic simulations of the processes under consideration. A 3D finite element model with a fine mesh in the weld and heat-affected zone is required for the estimation of welding residual stress, which is greatly

influenced by the type of heat source. The interaction between the material and the heat source, heat transport, and thermomechanical phase changes need to be described with greater accuracy for numerical modelling of the welding process.

2.1 Model geometry and material properties

On steel pipes with an inner diameter of 208 mm and a thickness of 5.6 mm, which resemble the primary sodium-carrying pipes in FBRs, the welding (circumferential) procedures have been simulated. The FEM technique has been used to model the TIG, A-TIG, laser, hybrid laser-TIG, and hybrid laser-MIG welding processes. In the weld area, a minimum element size of $0.46 \times 0.5 \times 2$ mm was used for accurate temperature distribution prediction. A larger element size is used outside the HAZ and weld zones. In Figure 1, the model is displayed.

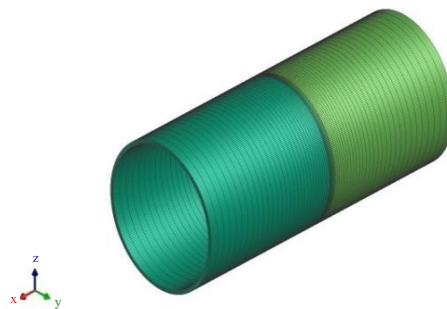


Figure 1. Finite element model in the butt joint configuration model

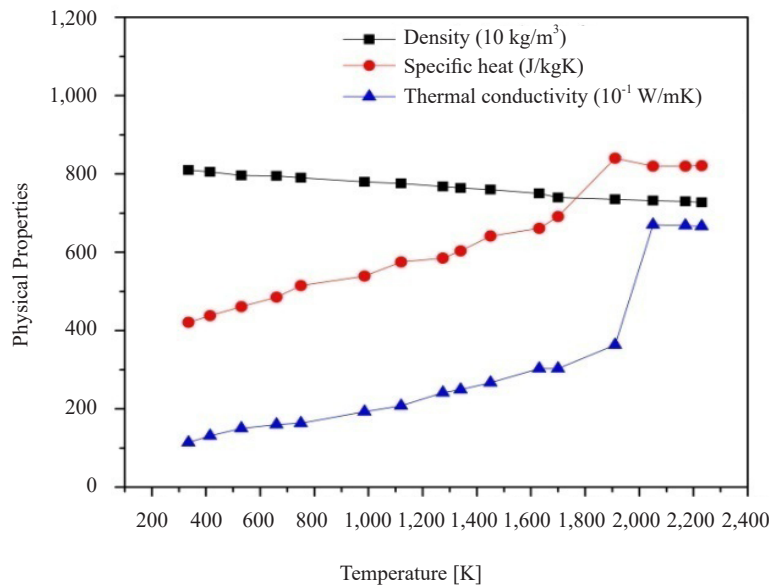


Figure 2. Thermophysical properties

The model's underlying presumptions are listed below.

- The fluid dynamics of the weld pool are not considered.
- To achieve the heat convection effect in the weld pool, increased thermal conductivity is used above the melting

point.

- Does not consider convection and fluid flow in the weld pool; ignores the influence of shielding gas on heat extraction.
 - On the basis of the weld bead dimensions transported from the weld crater at the end of the weld, weld geometry measurements can be approximated and fine-tuned.
 - The effects of the laser-arc interaction are not considered.
 - The filler material’s elemental constitution is similar to that of the base material.
- Figures 2 and 3 depict the mechanical and physical response of the parent material to temperature [46], [47].

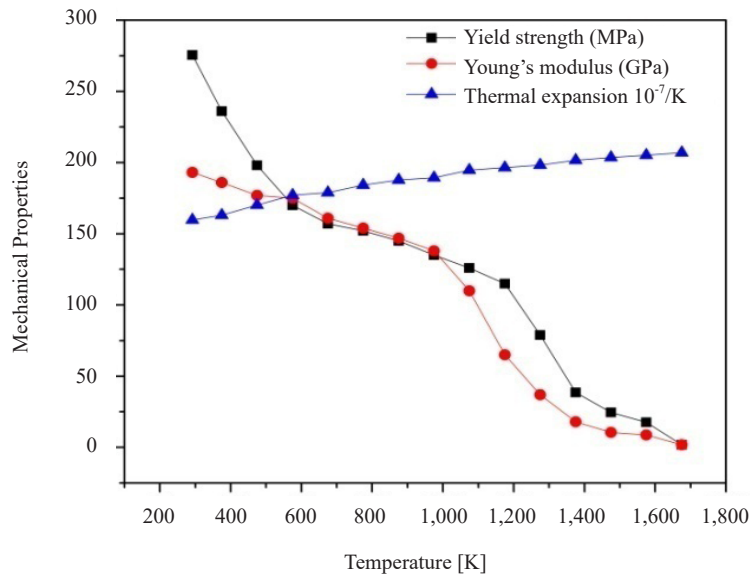


Figure 3. Thermomechanical properties

Incorporating the heat transfer effects arising from fluid flow within the molten pool is essential. Consequently, in the analysis, the thermal conductivity value was increased to 2-3 times above the melting temperature to accommodate the heat transfer caused by molten metal flow. Several researchers employed a similar approach to account for the heat transfer effects resulting from fluid flow [6], [36], [48]-[50].

2.2 Boundary conditions and governing equations

The initial temperature was 30 °C. The total heat losses are considered, including radiation heat loss in the weld pool, convective and conductive heat losses far from the weld pool, and additional heat losses. All of the model’s surfaces, except the symmetry plane, experienced convective and radiative losses. The welding pipes are suitably restrained to stop translational and rotational vibrations, similar to those in the lab.

When welding with restricted heating, most of the heat transfer occurs in the conduction mode. The thermophysical properties of the material, the amount of weld volume created, and the shape of the weld all affect the amount of heat is transferred. Heat conduction is defined by finding the solution to the underlying equation.

$$\nabla(k\nabla T) + Q = \rho C(\partial T / \partial t) \tag{1}$$

where, ρ is the density (kg/m³), C is the specific heat (J/kg °C), k is the thermal conductivity (W/m °C), and Q is the volumetric heat flux (W/m³). After welding, the molten material starts to cool to room temperature because of convection and radiation. The convection heat transfer rate is determined by Newton’s law of cooling equation [51].

2.3 Heat source modelling

The selection of an appropriate heat source model facilitates the precise estimation of the temperature distribution and weld bead shape. For the thermal analysis of the hybrid welding process, the combined heat source model was used. The most widely used double ellipsoidal heat source model was used for the TIG and A-TIG welding procedures [7], [51]-[53]. The laser heat source was modelled using a 3D conical and cylindrical shell [54]. Plate welds were used to calculate the physical weld bead parameters for the heat source model. Here the temperature-dependent thermophysical properties (Figure 2) were considered.

The double ellipsoidal heat source equations are as follows:

$$q_f = \frac{6\sqrt{3}f_f Q}{\pi a_f b c \sqrt{\pi}} \exp\left(\frac{-3(x-vt)^2}{a_f^2}\right) \exp\left(\frac{-3y^2}{b^2}\right) \exp\left(\frac{-3z^2}{c^2}\right) \quad (2)$$

$$q_r = \frac{6\sqrt{3}f_r Q}{\pi a_r b c \sqrt{\pi}} \exp\left(\frac{-3(x-vt)^2}{a_r^2}\right) \exp\left(\frac{-3y^2}{b^2}\right) \exp\left(\frac{-3z^2}{c^2}\right) \quad (3)$$

where a_f is the front length of the ellipsoid, a_r is the rear length, c is the depth of penetration, and b is the half width. The front and rear fractions of the heat source f_f and f_r , ($f_r + f_f = 2$), q_r and q_f are power densities (W/m^3) inside the front (f) and rear (r) half ellipsoids, respectively.

For the laser, the conical heat source model is given by the following equations,

$$Q_r = Q_0 e^{-\frac{r^2}{r_0^2}} \quad (4)$$

$$r = \sqrt{x^2 + y^2} \quad (5)$$

$$r_0 = r_e - \frac{(r_e - r_i)(z_e - z)}{z_e - z_i} \quad (6)$$

where Q_r is the heat source intensity, Q_0 is the maximum intensity, r_e and r_i are the surface radii in planes, and $z = z_e$ and $z = z_i$ correspondingly [6], [54]. Figures 2 and 3 represent all of a material's thermophysical and thermomechanical properties in relation to temperature. Figure 4 lists the heat source models employed in this research. It has been observed that the influence of the heat source characteristics varies for various welding situations. The width ' a ' and depth ' b ' parameters greatly increase their contribution to the model at lower weld current cases. However, the length parameter ' c ' contributed more than the other two as the power increased. The interaction between the width and depth parameters in both situations contributes significantly [55]. Weld joint fabrication and the parameters required for modelling were fully explored in our prior work by Ragavendran et al. [56]-[58]. When paired with laser welding process parameters, the heat source model may provide highly accurate stress variation prediction and deformation control during the welding process [59]. The heat source model for pipe welding simulation is fed with the corresponding welding parameters for each welding procedure.

3. Results and discussion

From the weld centerline, the temperature profile in the transverse direction is depicted. In the vicinity of the weldment, the generated peak temperature is nearly identical. Heat sources have no effect on distances further from the weldment. When the heat source moves along its trajectory during welding, the maximum temperature varies.

Since the heat source hits a respective node and continues to cool as it moves further, all of the nodes are heated to their maximum temperature. All thermal cycles, fusion geometry, and residual stress profiles generated by the welding processes are provided at the location with 180° central angle. With the exception of the temperature histories at the weld start/endpoint with a 0° central angle, the other three temperature histories at 90° , 180° , and 270° locations have almost identical cycles in shape and magnitude. Figure 5 shows the TIG weld model and temperature distribution in 3D model. In the quasi-state scenario, the profiles are acquired. The temperature contour of TIG welding is shown in Figure 6 and the validated profile is presented in Figure 7. The simulated pipe welded using the TIG welding process is shown in Figure 8. The thermal cycles observed in the TIG welding process are presented in Figure 9.

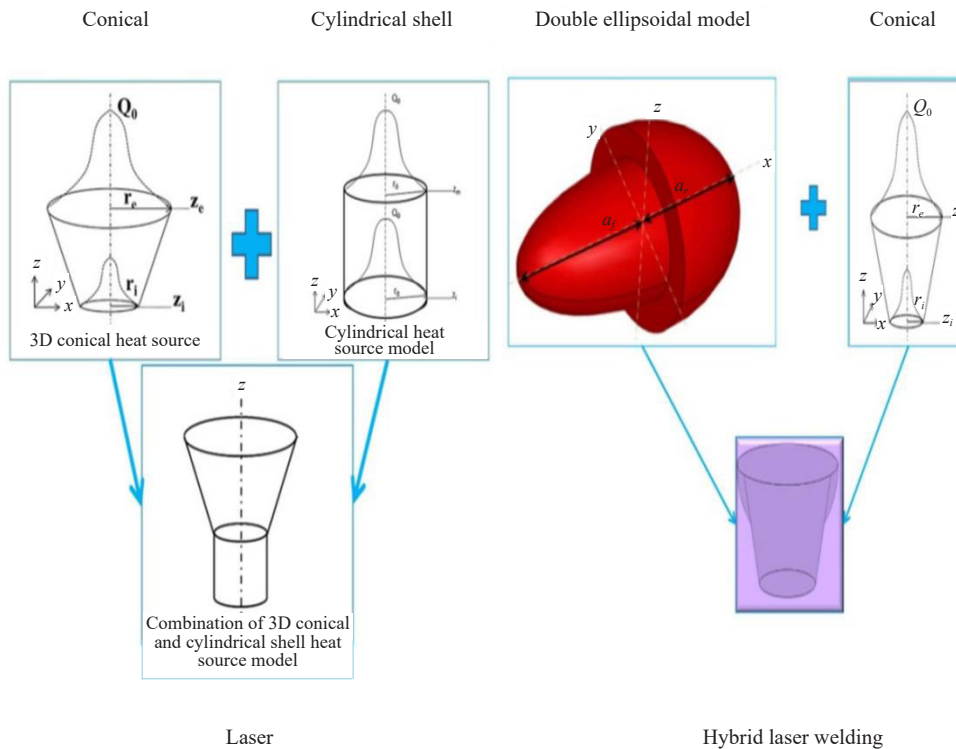
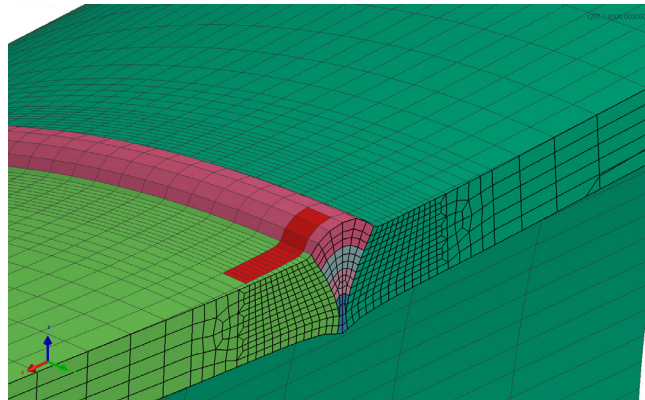
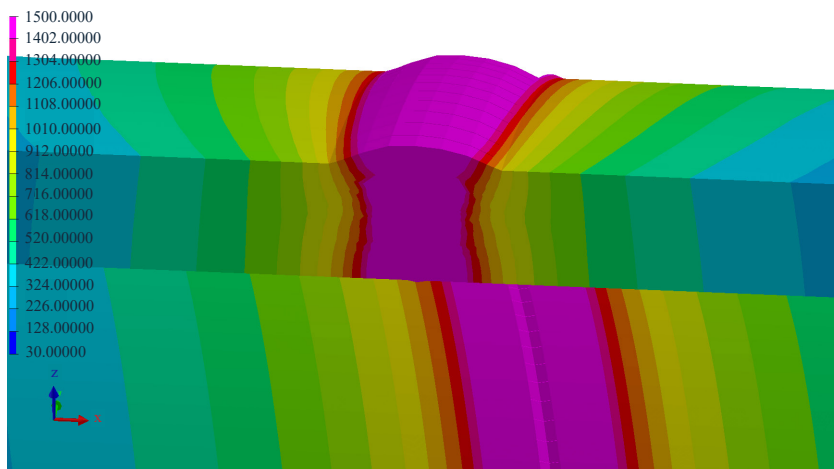


Figure 4. Heat source models

The predicted residual stress profiles for TIG pipe joints at the inner and outer diameter are presented in Figure 10 and Figure 11. The TIG weld macrograph exhibited the highest weld metal volume due to the incorporation of filler wire and groove design. The tensile stress distribution width is higher with the TIG joint because of the application of multiple thermal cycles to fill the groove with high heat input. The peak temperature exhibited in the top pass of the TIG weld joint was $2,219^\circ\text{C}$. The hoop residual stress values at the weld centre are always higher than the axial residual stress in the internal diameter. The residual stress in the external diameter is always lower than in the internal diameter side. At the inner diameter, the axial stress is lower than the hoop stress, and the peak axial stress values are within the yield strength limit of the material. The tensile axial stress has a broader distribution than the tensile hoop stress at the inner diameter. The tensile axial stress at the weld centre is lower than that in the adjacent regions due to the strain hardening and high-temperature gradient associated with more thermal strains produced by high heat input of the TIG welding. The axial stress is compressive at the weld centre in the outer diameter, whereas the hoop stress is tensile. Apart from the weld centre, the tensile hoop stress values are lower than the axial stress values.



(a)



(b)

Figure 5. a) TIG weld model and b) temperature distribution in 3D model

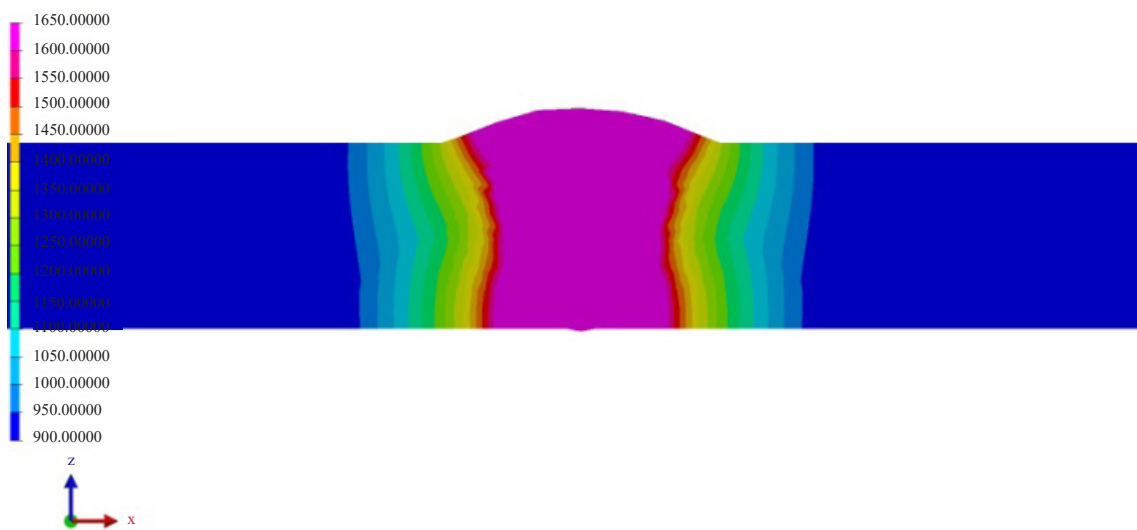


Figure 6. Predicted TIG weld macrograph

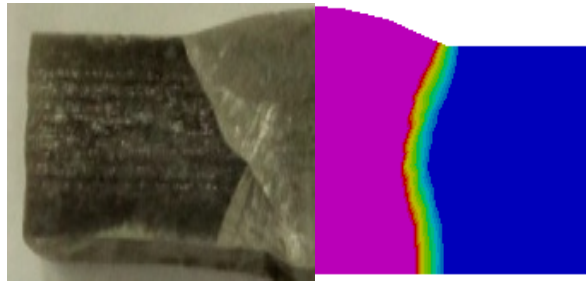


Figure 7. Validated TIG weld macrograph

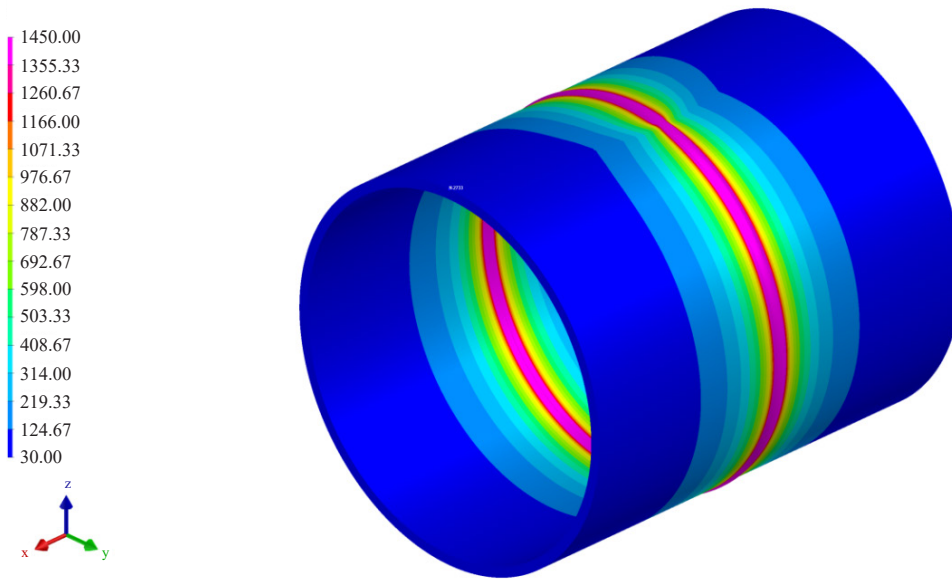


Figure 8. Simulated pipe welded using the TIG welding process

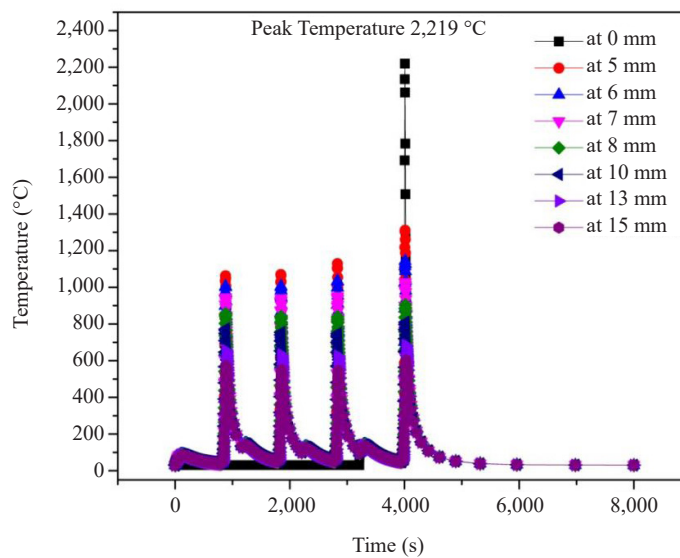


Figure 9. Thermal cycles for the TIG weld joint

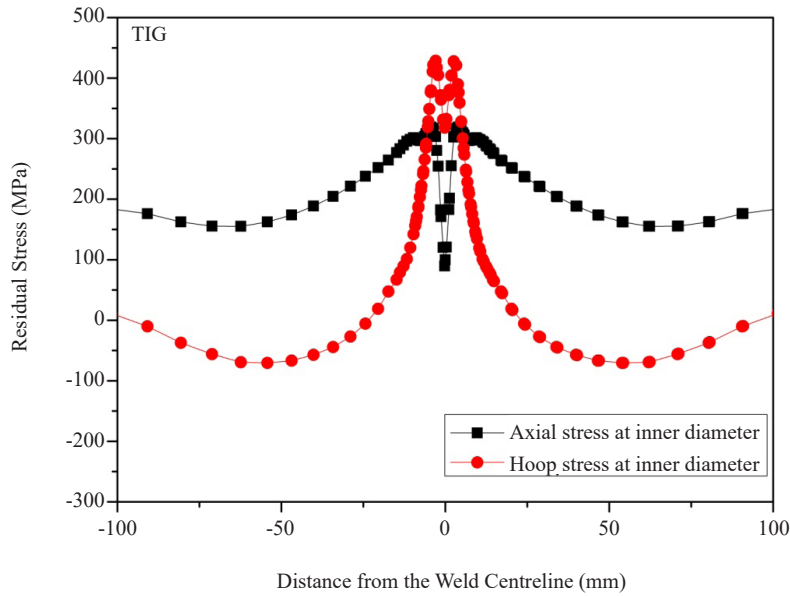


Figure 10. Predicted residual stress distribution across the pipe in the TIG at the inner diameter

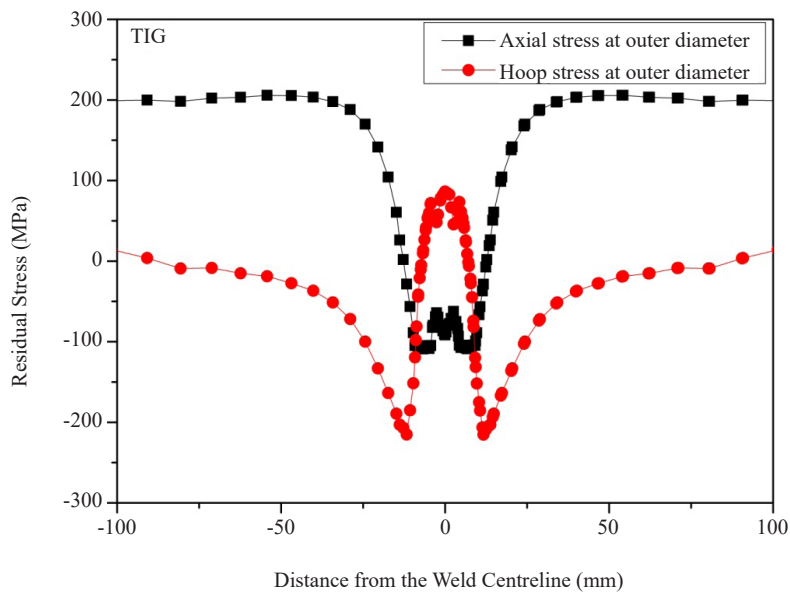


Figure 11. Predicted residual stress distribution across the pipe in the TIG at the outer diameter

The temperature contour, temperature distribution, and residual stress prediction for A-TIG pipe welding simulation are given in Figures 12-16. The A-TIG weld metal exhibited lower volume among the arc welding processes than the TIG weld metal. The peak temperature determined in A-TIG weld joint is 1,650 °C. For A-TIG, no groove preparation is required. Due to this reduced restraint in A-TIG, the tensile residual stress dispersion is lower than in the TIG welding process. At the inner diameter, the axial stress values are higher than the hoop stress values for the A-TIG joint - the maximum residual stress values are within the yield limits. Axial stresses are fully compressive at the weld centre, and hoop stresses are almost compressive at the outer diameter. Away from the weld, the axial stress values are more significant than the hoop stress values.

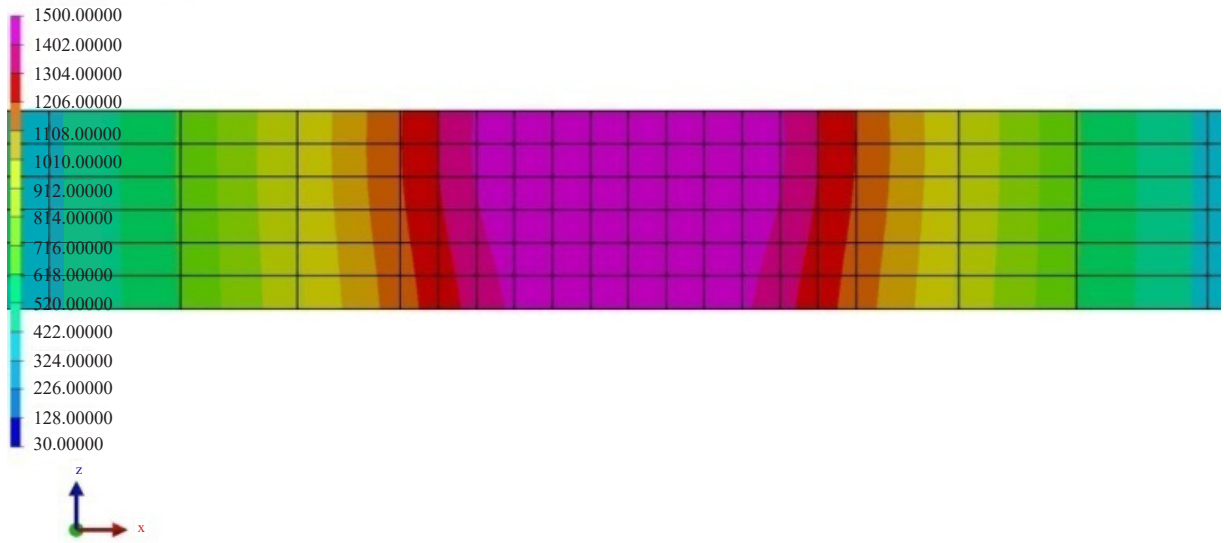


Figure 12. Predicted A-TIG weld macrograph

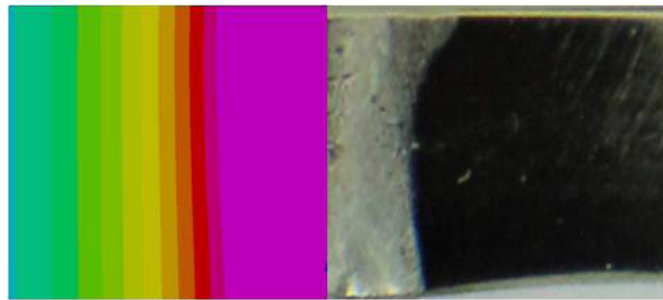


Figure 13. Validated A-TIG weld macrograph

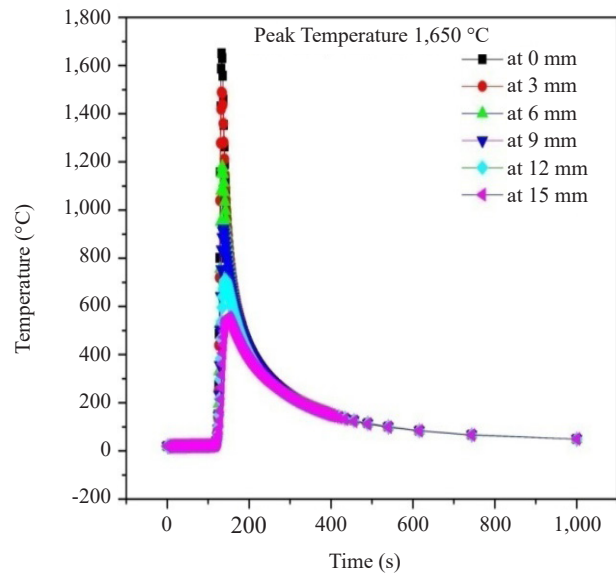


Figure 14. Predicted temperature distribution across the pipe in A-TIG weld joint

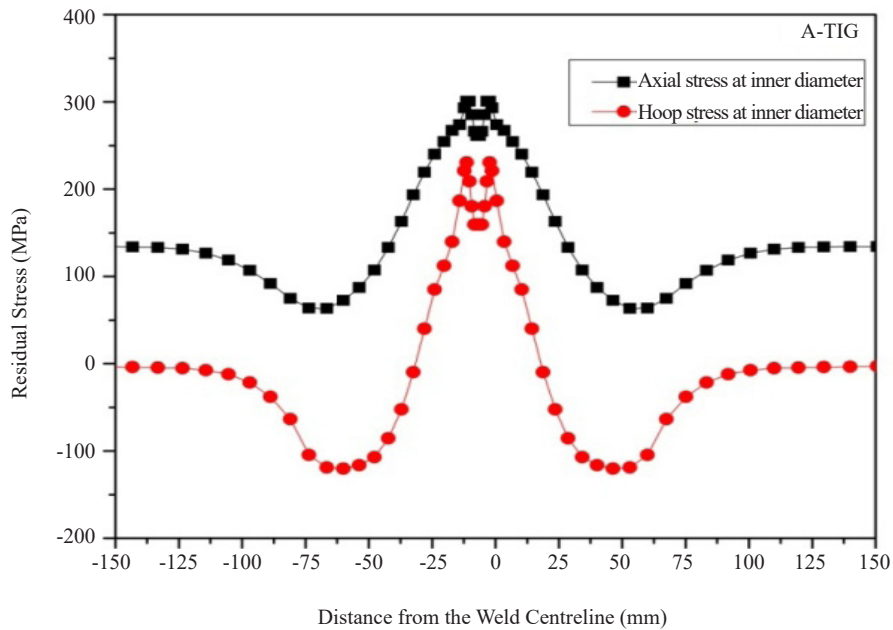


Figure 15. Predicted residual stress distribution across the pipe in the A-TIG at the inner diameter

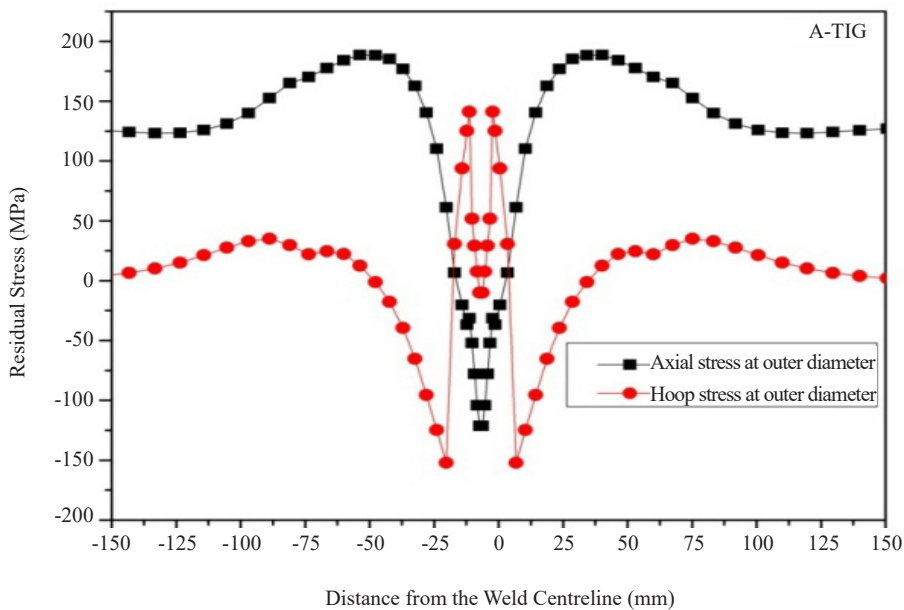


Figure 16. Predicted residual stress distribution across the pipe in the A-TIG at the outer diameter

The laser welding simulation results are given below. The laser weld contour is shown in Figure 17, and the validated profile is shown in Figure 18. The thermal cycles observed in laser welding are shown in Figure 19. The laser weld exhibited a narrow weld metal volume among all the weld joints owing to the maximum power density associated with the laser beam. The peak temperature manifested in the laser weld joint is 2,187 °C. This process exhibited the rapid cooling rate because of a high heat sink and lower heat input. The increased amount of tensile residual stress in the laser weld is due to the low heat input associated with the laser heat source.

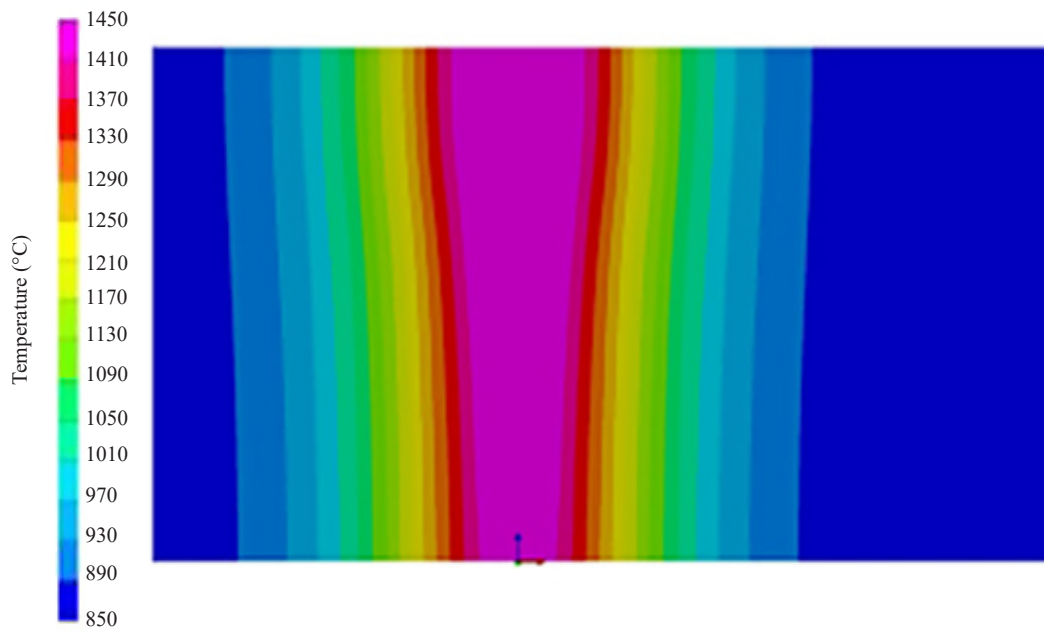


Figure 17. Predicted laser weld macrograph



Figure 18. Validated laser weld macrograph

The higher hoop residual stress in the laser weld is due to the narrow weld bead geometry and the greater longitudinal constraint. At the inner diameter, the hoop stress values are greater than the axial stress at the weld centre in the laser weld joint. The axial stress is completely compressive at the weld centre at the outer diameter, whereas the hoop stress is tensile. The tensile stress distribution is narrow in the case of the laser joint due to low heat input.

However, at the same time, the hoop stress values are above the yield strength of the material due to a sharp temperature gradient, which aids in the formation of peak tensile hoop stress at the welds. Figure 20 and Figure 21 show the residual stress spread across the laser weld joint at the inner and outer diameters.

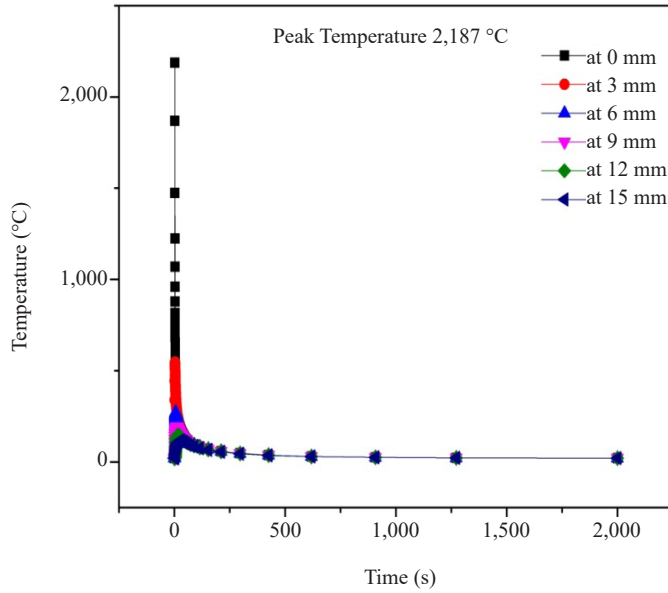


Figure 19. Predicted temperature distribution across the pipe in laser weld joint

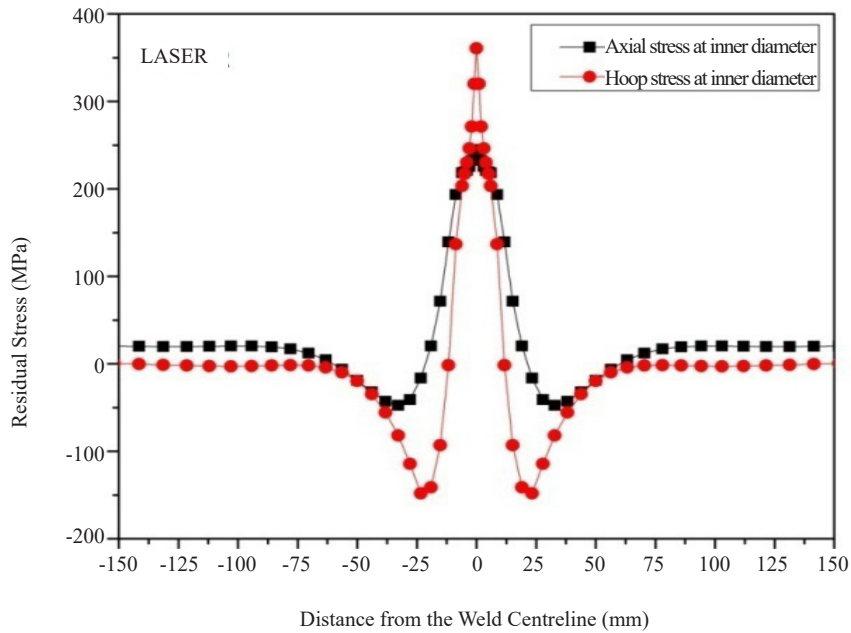


Figure 20. Predicted residual stress distribution across the pipe in the laser weld at the inner diameter

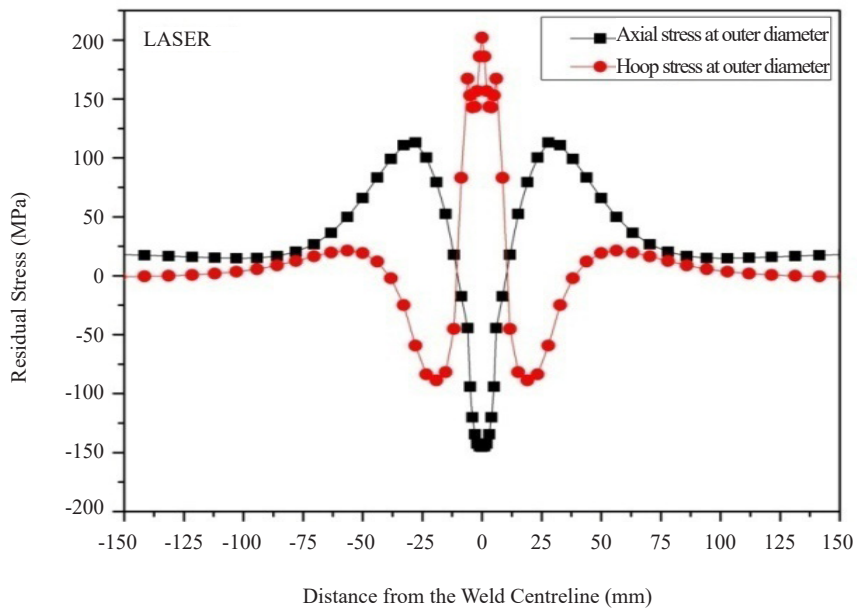


Figure 21. Predicted residual stress distribution across the pipe in the laser weld at the outer diameter

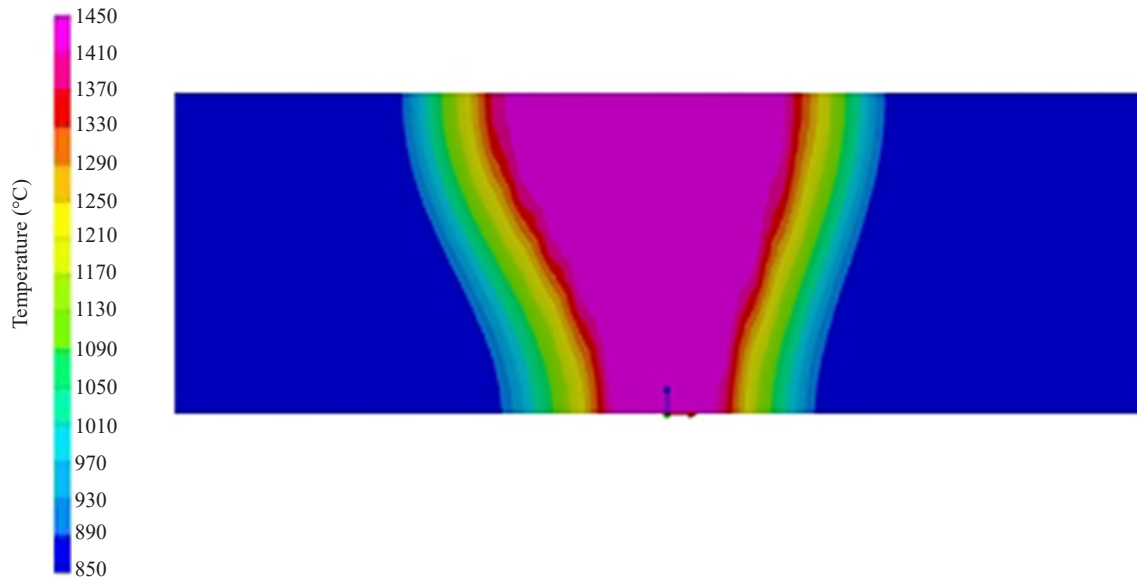


Figure 22. Predicted hybrid laser-TIG weld macrograph

The hybrid laser TIG welding simulation results are shown from Figures 22-26. In this process, the weld is made of a single pass, and a hybrid heat source is used in which the laser source influences the hoop stress. The hybrid laser-TIG weld exhibited a distinctive weld geometry; the top portion was entirely controlled by the TIG source and the root portion by a laser. The peak temperature indicated in the hybrid laser-TIG weld joint is 2,103 °C.

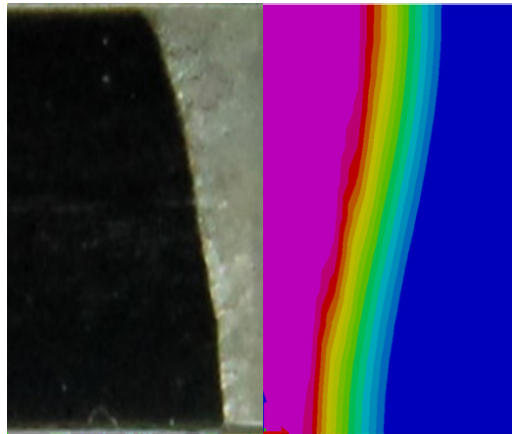


Figure 23. Validated hybrid laser-TIG weld macrograph

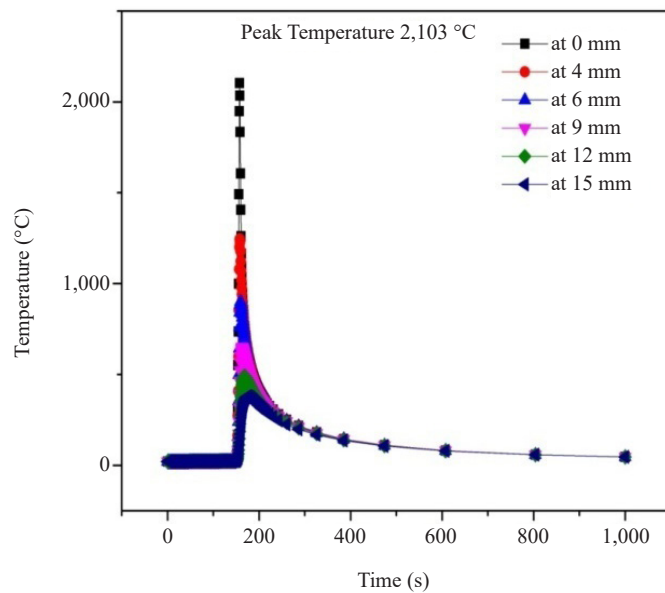


Figure 24. Predicted temperature distribution across the pipe in the hybrid laser-TIG weld joint

The hybrid laser-MIG welding simulation results are shown below from Figures 27-31. In this process configuration, the laser is leading, the keyhole is produced by the laser, and the top portion is fully influenced through the MIG source. The hybrid laser-MIG weld joint exhibited a distinctive wine cup-shaped weld. The peak temperature manifested in the laser weld joint is 3,421 °C. The cooling rate of this process is higher than those of the hybrid laser-TIG and arc-based TIG and A-TIG processes. The tensile stress distribution is narrower than that of the hybrid laser-TIG welding. The peak hoop stress values at the inner diameter are higher than the peak axial stress values at the weld centre. Moreover, like all processes, away from the weld centre, the axial stress has a slightly broader and higher tensile stress than the hoop stress at the internal and external diameter. The peak tensile hoop stress at the weld centre is greater than the yield strength of the material. At the outer diameter, the axial stress in the weld centre is compressive, whereas the hoop stress is tensile.

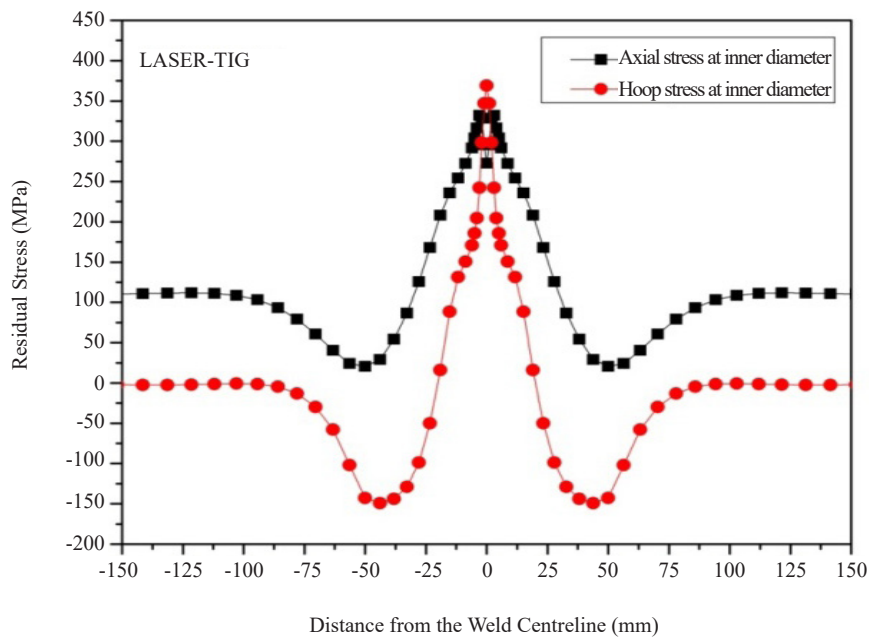


Figure 25. Predicted residual stress distribution across the pipe in the hybrid laser-TIG weld at the inner diameter

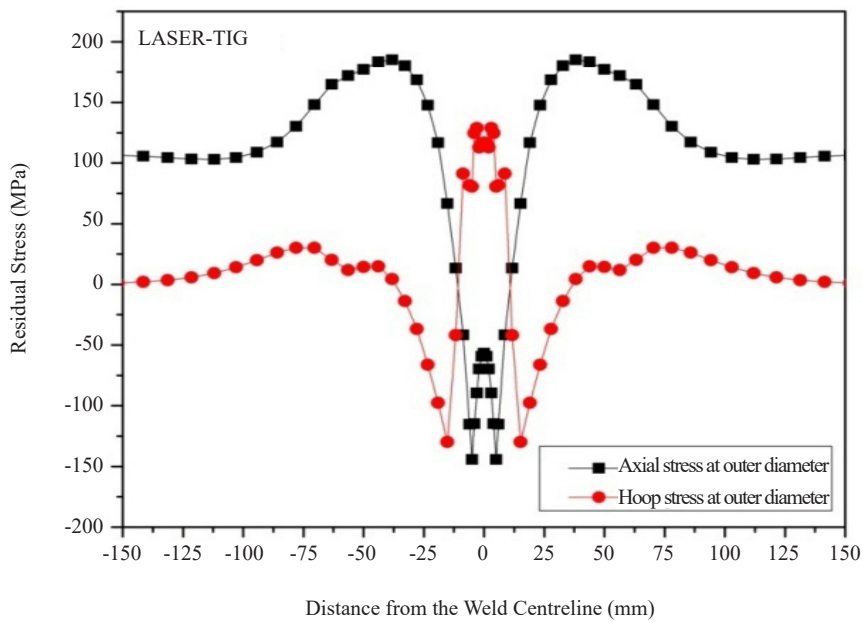


Figure 26. Predicted residual stress distribution across the pipe in the hybrid laser-TIG weld at the outer diameter

At the inner diameter, similar to the laser weld joint, the hybrid laser-TIG weld joint exhibited a higher maximum tensile hoop stress in the weld centre. Moreover, the hoop stress distribution is narrower than the axial stress at the inner diameter. The axial stress values are compressive at the external diameter, whereas the hoop stress values are tensile. Far from the weld, the hoop stress values are nearly compressive; in contrast, the axial stress values are tensile at the outer diameter.

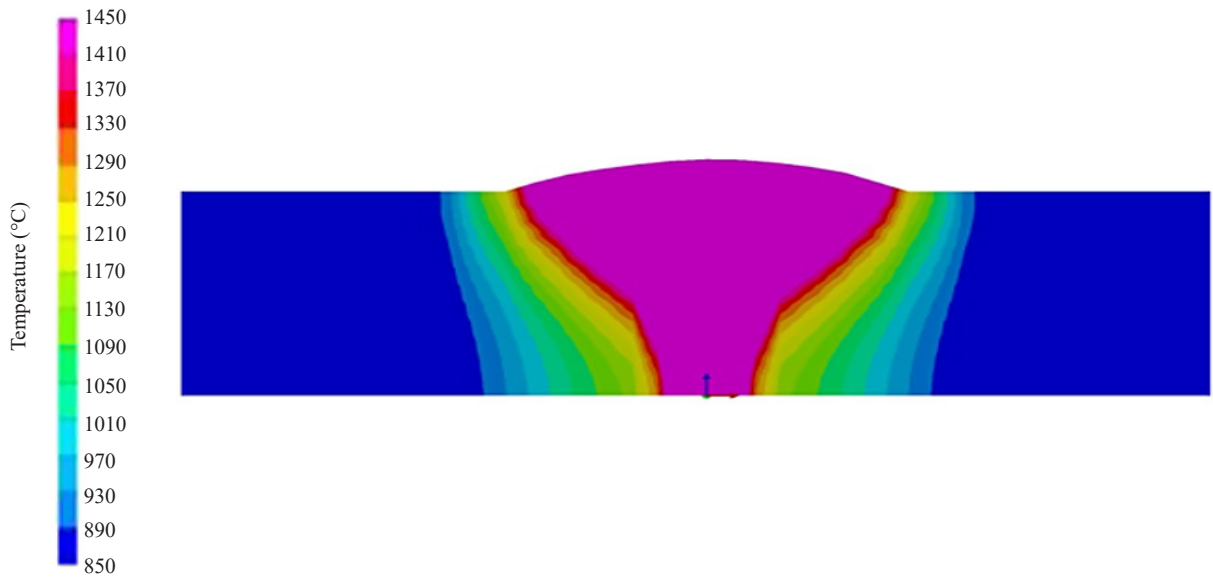


Figure 27. Predicted hybrid laser-MIG weld macrograph

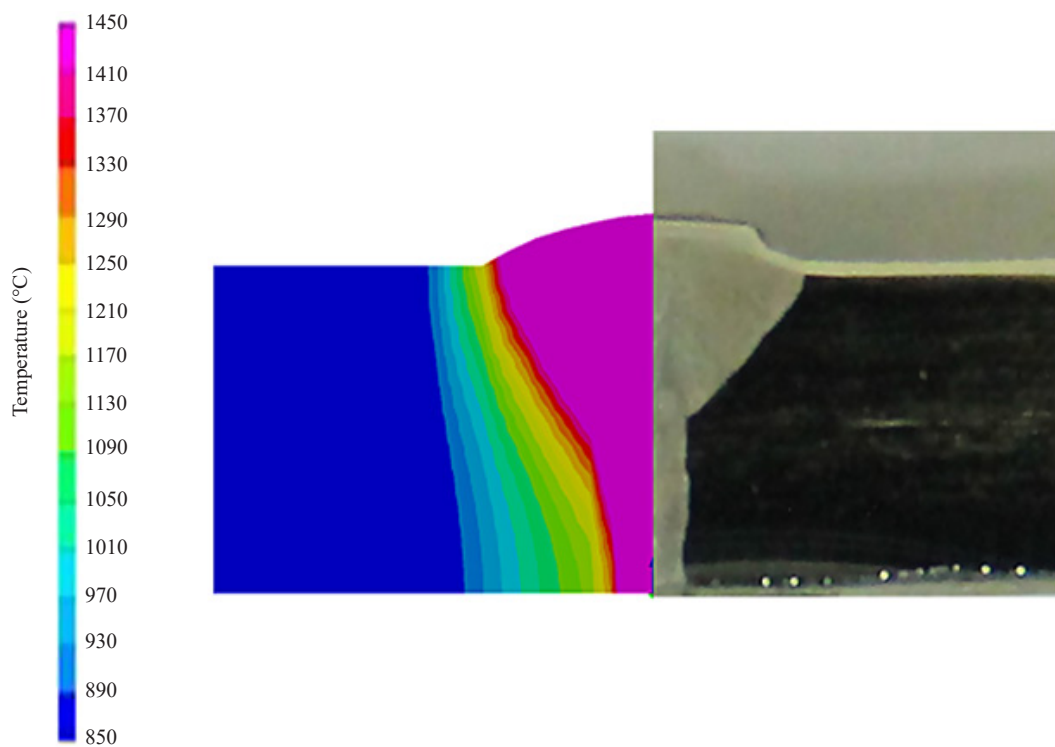


Figure 28. Validated hybrid laser-MIG weld macrograph

Table 1 shows the welding processes heat input, the peak temperature-induced by welding, and the associated cooling rates. The total heat input associated with the TIG process is 2.84 kJ/mm, and the average heat input per pass for the TIG process is 0.71 kJ/mm.

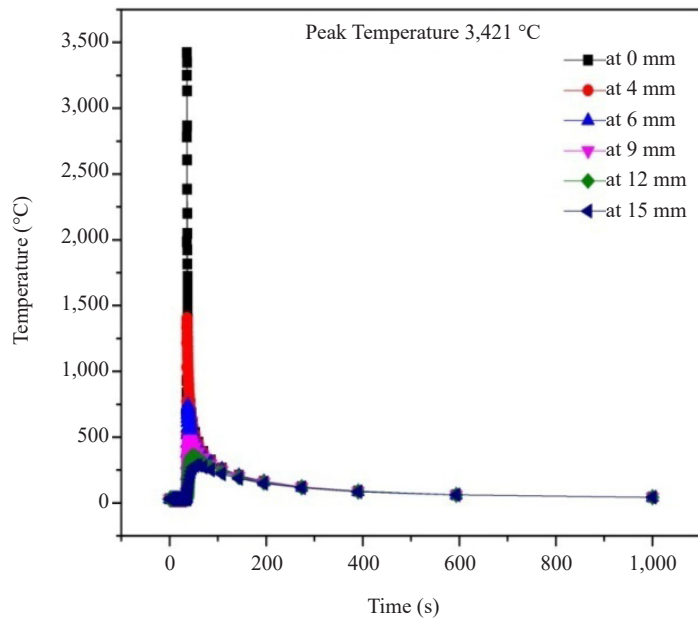


Figure 29. Predicted temperature distribution across the pipe during hybrid laser-MIG welding

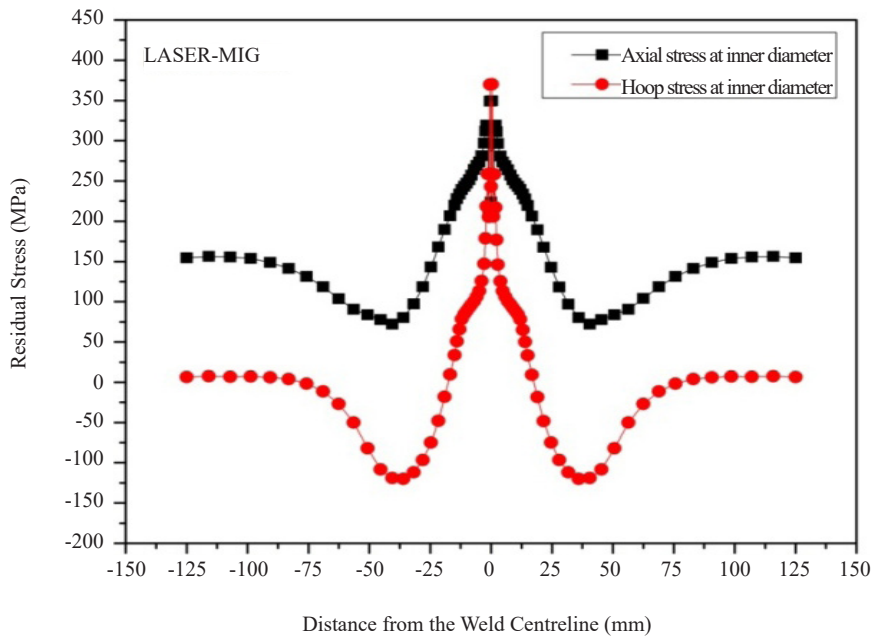


Figure 30. Predicted residual stress distribution across the pipe in the hybrid laser-MIG weld at the inner diameter

The predicted axial residual stress dispersal across all the 316LN pipe weld joints at inner diameter is shown in Figure 32. From this, it was observed that the peak residual stress values are all of the order of yield strength of the base material. The width of the tensile residual stress distribution aligns with the heat input applied to produce the joints. The greater the heat input employed, the higher is the tensile residual stress width. Therefore, the arc-based joints presented a higher tensile stress distribution width than the laser-based welding processes.

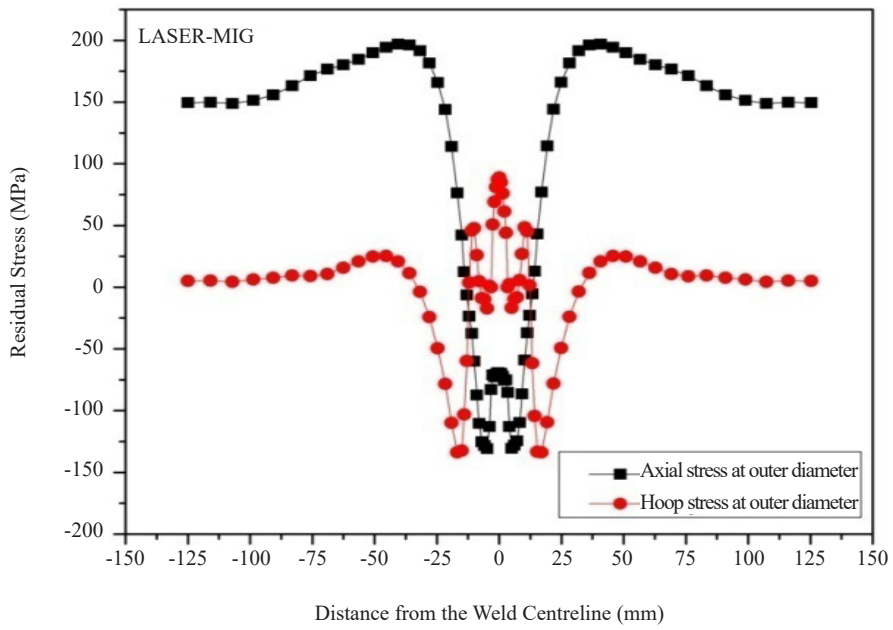


Figure 31. Predicted residual stress distribution across the pipe in the hybrid laser-MIG weld at the outer diameter

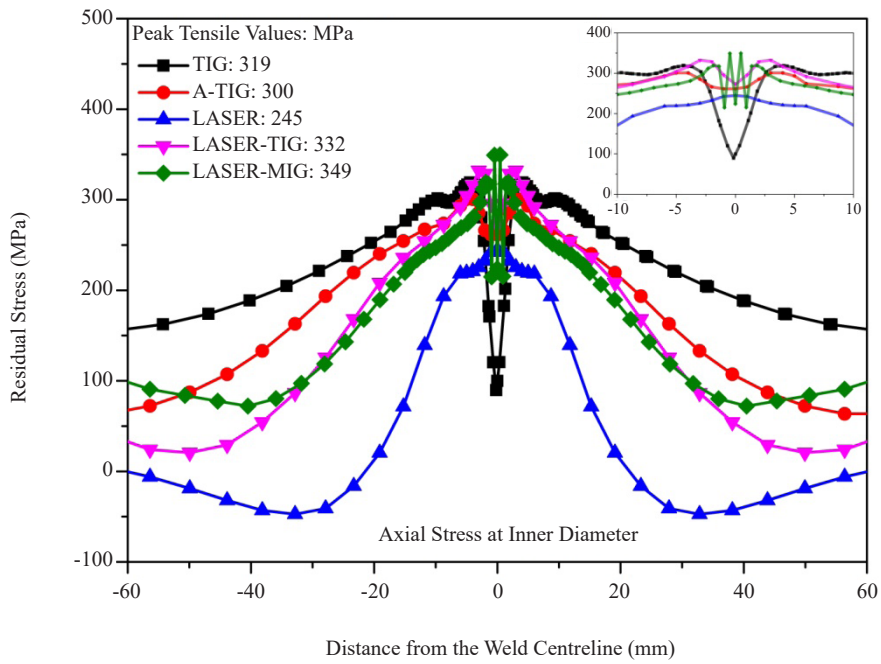


Figure 32. Predicted axial residual stress distribution across the 316LN pipe weld joints at the inner diameter

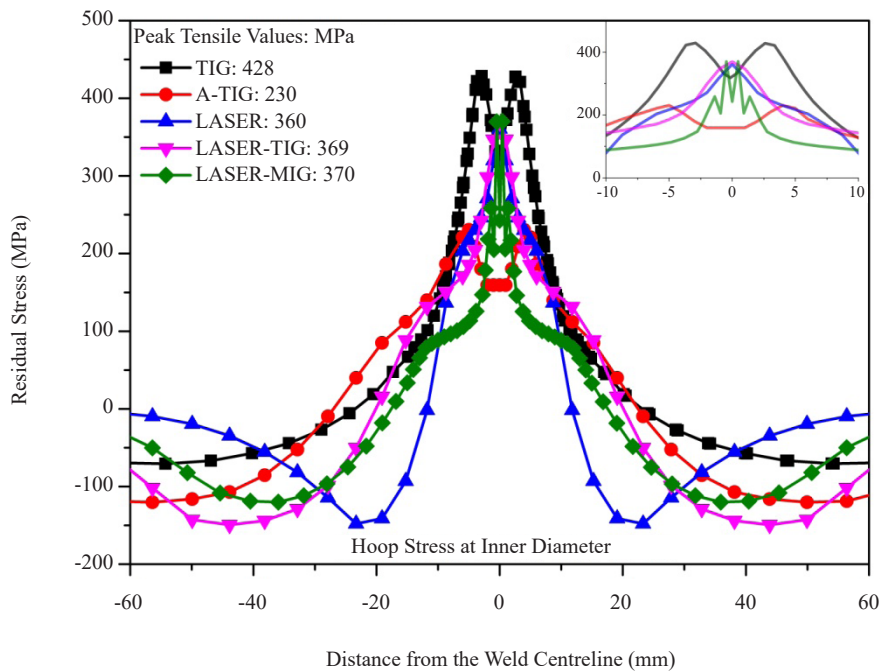


Figure 33. Predicted hoop residual stress distribution across the 316LN pipe weld joints at the inner diameter

Table 1. Thermal results of welding processes

S. No	Welding process	Total heat input (kJ/mm)	Peak temperature (°C)	Cooling rate (°C/s)
1	TIG	0.71	2,219	6.8
2	A-TIG	0.98	1,650	9.5
3	Laser	0.12	2,187	195.5
4	Laser-TIG	0.41	2,103	15.9
5	Laser-MIG	0.28	3,421	25.4

The predicted hoop residual stress distribution across all the 316LN pipe weld joints at inner diameter is shown in Figure 33. From this, it was found that the TIG joint revealed the highest hoop stress than the other joints. All the laser-based joints exhibited the same amount of peak hoop tensile stress on the inner side, which is entirely influenced by the laser. Among the joints, A-TIG showed the lowest hoop tensile residual stress than the other joints.

The predicted axial residual stress distribution across all the 316LN pipe weld joints at outer diameter is shown in Figure 34. At the weld centre, all the pipe weld joints manifested the compressive residual stress, away from the weld joints exhibiting the tensile residual stress, which is lower than the yield strength of the material.

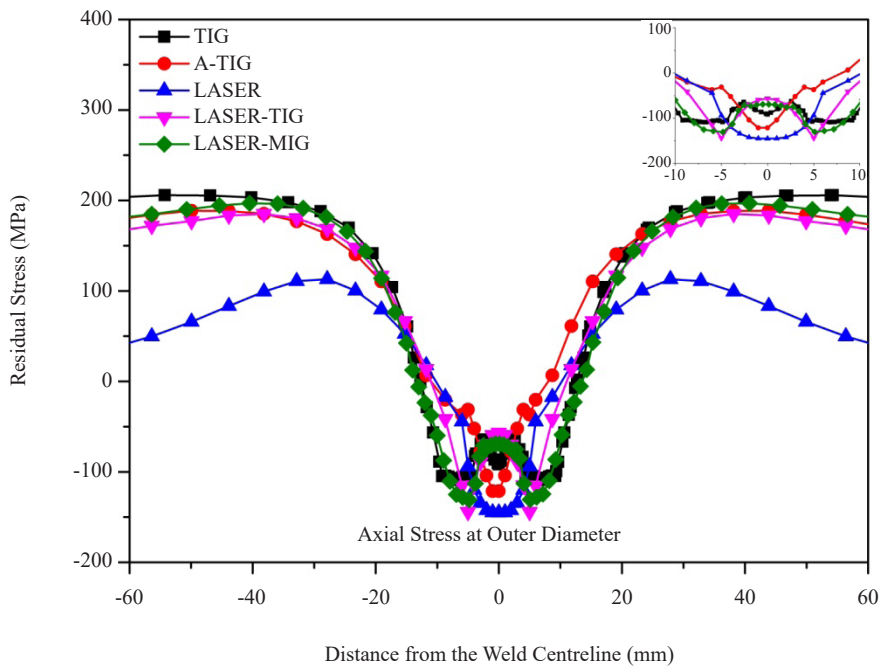


Figure 34. Predicted axial residual stress distribution across the 316LN pipe weld joints at the outer diameter

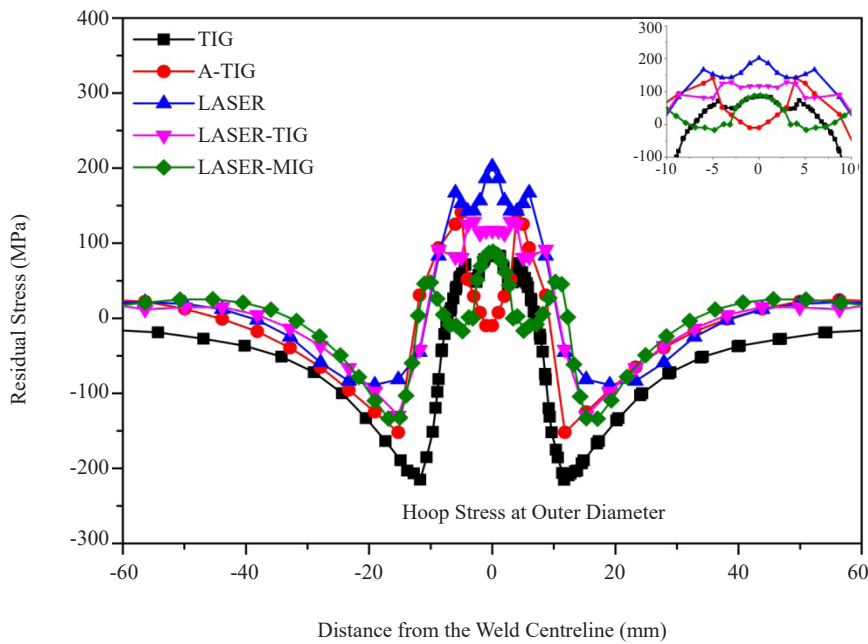


Figure 35. Predicted hoop residual stress distribution across the 316LN pipe weld joints at the outer diameter

The predicted hoop residual stress distribution across all the 316LN pipe weld joints at outer diameter is shown in Figure 35. It is observed that the laser joint exhibited the highest peak tensile hoop stress at the outer diameter than the other joints. The higher hoop stress is due to the constraint, thermal shock and rapid cooling rate of the laser welding process. At the outer diameter, the peak hoop residual stress values are lower than the yield strength of the material. A-TIG

joint shown the lowest hoop stress among all the pipe weld joints.

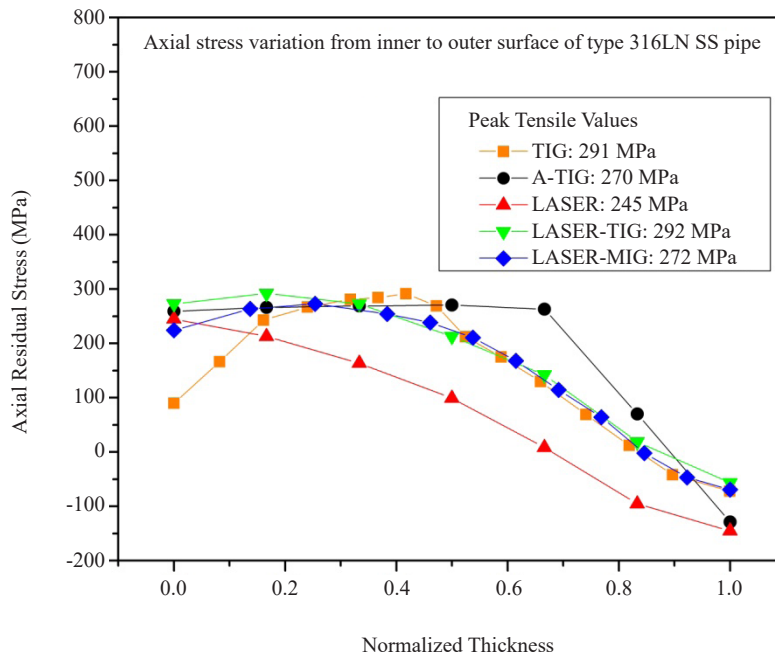


Figure 36. Axial stress variations from the inner to the outer surface of type 316L(N) stainless steel weld joints

The hoop and axial stress distribution across the weld centerline at the inner and outer diameter in the present study (the axial stresses are tensile at the inner surface, whereas the stress is compressive in nature at the outer surface. But the hoop stress at the weld in both the top and bottom surfaces are tensile) are similar and agreeing with the results presented by Deng and Kiyoshima [31].

In general, both plate and pipe weld joints exhibit residual stresses due to the inhibition of thermal contraction caused by the processes and the weld joint configurations. However, it was demonstrated that the self-constraining tubular shape results in a stress state that is markedly different from that observed in plates, which are discussed in our previous work [60]. This is especially true for stresses transverse to the weld joint, i.e., in the axial direction of the pipes, which are compressive on the outside and tensile on the inside. Whereas hoop residual stresses in tubular welds are equivalent to longitudinal stresses in plates, axial residual stresses are not. The significant amount compressive stresses are most noticeable around the weld toe and can only be found to a minimal extent in welded plates. The tubular shape explains the large discrepancy. Because the degree of confinement in welded plates is substantially lower than in pipes, the transverse residual stresses are relatively modest. The controlling mechanism for these effects is a circumferential shrinkage of the weld joint, which may cause pipe necking and pipe wall bending. On cooling, the weld joint shrinks circumferentially, generating a radial contraction or necking of the pipe. The resulting bending of the pipe wall creates axial stresses that are compressive near the weld joint and tensile at distances greater than 20 mm at the outer surface. The obtained outcomes are in agreement with the work of Hempel et al. [61].

The axial stress and hoop stress variation from inner to outer surface (in through thickness direction) is shown in Figure 36 and Figure 37. From these, it is observed that the axial stress values are within the yield stress limit and at the outer surface the axial stress at all the welds are compressive in nature. The hoop stresses are more detrimental in pipes than the axial residual stress because it promotes earlier crack initiation and easier crack propagation in welds. Laser welding results in higher amount of hoop residual stress in weld joints when compared to other welding processes.

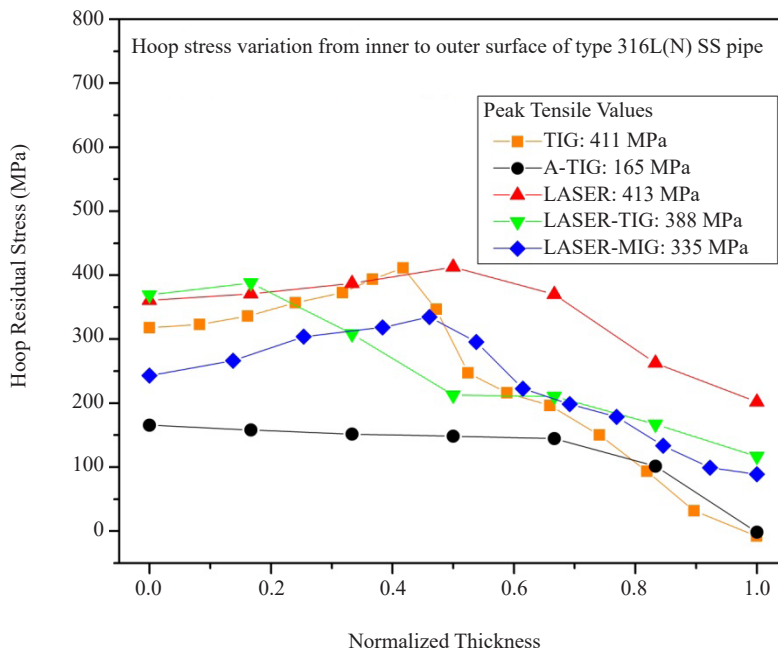


Figure 37. Hoop stress variation from inner to outer surface of type 316L(N) stainless steel weld joints

4. Conclusion

The effect of various welding processes on the residual stress induced in 316L(N) stainless steel pipes of inner diameter 208 mm with thickness 5.6 mm resembling the primary sodium transporting pipes in FBRs is studied in the present work. Numerical modelling was used to explore the residual stress state prediction on the internal and external surfaces of butt-welded pipe joints. The conclusions are given below.

- Laser pipe weld joint exhibited the highest tensile hoop stress value of 413 MPa and a hoop stress value of over 200 MPa at the outer diameter. Presence of higher hoop stress values at the outer diameter may lead to cracking and premature failure of the pipe weld joint. Similarly, hybrid laser-arc weld joints exhibited higher tensile hoop stress values at the outer diameter.
- Conventional TIG pipe weld joint exhibited a hoop tensile residual stress value of over 300 MPa at the inner diameter. However, at the outer diameter the hoop residual stresses are compressive in nature. TIG pipe weld joint exhibited a large gradient in residual stress values from inner to outer diameter.
- A-TIG weld joint has exhibited lower hoop stress of 165 MPa at the inner diameter and -2 MPa at the outer diameter. Also there is no large gradient in residual stress variation from inner to outer diameter.
- The lowest residual hoop stress observed in A-TIG welded pipe joint is due to the straight-sided weld bead, lower maximum temperature and slow cooling rate.

Therefore, among the welding processes chosen in the present study, A-TIG welding is recommended for welding of 316L(N) stainless steel primary sodium carrying pipes in FBR.

Acknowledgement

The authors are thankful to the ARCI-Hyderabad, India, for extending their facility to carry out the work. Mr D Manokaran and Mr S Arun Kumar are gratefully acknowledged for their tremendous help and support. One of the authors, Mr M. Ragavendran, thanks the Department of Atomic Energy (DAE), India, for granting the fellowship.

Funding

This research did not receive any specific grant from funding agencies in the public, commercial, or not-for-profit sectors.

Conflict of interest

The authors declare no competing financial interests.

References

- [1] P. J. Bouchard, "Validated residual stress profiles for fracture assessments of stainless steel pipe girth welds," *International Journal of Pressure Vessels and Piping*, vol. 84, no. 4, pp. 195-222, 2007.
- [2] H. Djeloud, M. Moussaoui, R. Kouider, A. Al-Kassir, and J. P. Carrasco-Amador, "Study of the heat exchange and relaxation conditions of residual stresses due to welding of austenitic stainless steel," *Energies (Basel)*, vol. 16, no. 7, 2023.
- [3] Q. Chen, J. Yang, X. H. Liu, J. L. Tang, and B. H. Huang, "Effect of the groove type when considering a thermometallurgical-mechanical model of the welding residual stress and deformation in an S355JR-316L dissimilar welded joint," *Journal of Manufacturing Processes*, vol. 45, pp. 290-303, 2019.
- [4] S. W. Wen, P. Hilton, and D. C. J. Farrugia, "Finite element modelling of a submerged arc welding process," *Journal of Materials Processing Technology*, vol. 119, no. 1-3, pp. 203-209, 2001.
- [5] W. Jiang, Y. Zhang, and W. Woo, "Using heat sink technology to decrease residual stress in 316L stainless steel welding joint: Finite element simulation," *International Journal of Pressure Vessels and Piping*, vol. 92, pp. 56-62, 2012.
- [6] A. R. Pavan, B. Arivazhagan, M. Vasudevan, and G. K. Sharma, "Numerical simulation and validation of residual stresses and distortion in type 316L(N) stainless steel weld joints fabricated by advanced welding techniques," *CIRP Journal of Manufacturing Science & Technology*, vol. 39, pp. 294-307, 2022.
- [7] A. R. Pavan, B. Arivazhagan, G. K. Sharma, S. A. Kumar, S. Mahadevan, and M. Vasudevan, "Influence of hardening models on the estimation of residual stresses by finite element modeling in type 316LN stainless steel weld joints," *Journal of Materials Engineering and Performance*, vol. 31, no. 9, pp. 6988-6997, 2022.
- [8] H. Vemanaboina, S. Akella, R. K. Buddu, B. Yelamasetti, M. B. Matam, K. H. Salem, K. K. Saxena, C. Prakash, and D. Buddhi, "Prediction of thermal and residual stress distributions in SS304 materials for nuclear application using finite element analysis," *International Journal on Interactive Design and Manufacturing (IJIDeM)*, 2023.
- [9] S. Das Banik, S. Kumar, P. K. Singh, and S. Bhattacharya, "Influence of weld repair on the residual stresses induced in austenitic stainless steel weld joints," *Production Engineering*, vol. 17, no. 1, pp. 81-94, 2023.
- [10] X. F. Kong, X. Wang, B. C. Lin, Z. L. Xiong, X. Y. Deng, X. Li, and Y. X. Lu, "Innovative prevention of stress corrosion crack propagation in nuclear power pipe welds," *Materials Testing*, vol. 65, no. 8, pp. 1145-1154, 2023.
- [11] R.-F. Liu and J.-C. Wang, "Application of finite element method to effect of weld overlay residual stress on probability of piping failure," *International Journal of Pressure Vessels and Piping*, vol. 200, pp. 104812, 2022.
- [12] T. T. Nguyen, V. S. Pham, H. A. Tran, D. H. Nguyen, T. H. Nguyen, and H. B. Dinh, "Effect of residual stress on mode-I stress intensity factor: A quantitative evaluation and a suggestion of an estimating equation," *Metals (Basel)*, vol. 13, no. 6, pp. 1132, 2023.
- [13] F. Miyasaka, Y. Yamane, and T. Ohji, "Development of circumferential TIG welding process model: A simulation model for welding of pipe and plate," *Science and Technology of Welding and Joining*, vol. 10, no. 5, pp. 521-527, 2005.
- [14] S. Li, J. Li, G. Sun, and D. Deng, "Modeling of welding residual stress in a dissimilar metal butt-welded joint between P92 ferritic steel and SUS304 austenitic stainless steel," *Journal of Materials Research and Technology*, vol. 23, pp. 4938-4954, 2023.
- [15] P. Duranton, J. Devaux, V. Robin, P. Gilles, and J. M. Bergheau, "3D modelling of multipass welding of a 316L stainless steel pipe," *Journal of Materials Processing Technology*, vol. 153-154, pp. 457-463, 2004.
- [16] J. Xu, X. Jia, Y. Fan, A. Liu, and C. Zhang, "Residual stress analyses in a pipe welding simulation: 3D pipe versus axi-symmetric models," *Procedia Materials Science*, vol. 3, pp. 511-516, 2014.

- [17] D. K. Rissaki, P. G. Benardos, G.-C. Vosniakos, M. C. Smith, and A. N. Vasileiou, "Residual stress prediction of arc welded austenitic pipes with artificial neural network ensemble using experimental data," *International Journal of Pressure Vessels and Piping*, vol. 204, pp. 104954, 2023.
- [18] M. Vafaei, A. Mashhuriazar, H. Omidvar, and Z. Sajuri, "In-service welding of X70 steel gas pipeline: Numerical and experimental investigations," *Journal of Materials Research and Technology*, vol. 26, pp. 6907-6918, 2023.
- [19] D. Deng and H. Murakawa, "Numerical simulation of temperature field and residual stress in multi-pass welds in stainless steel pipe and comparison with experimental measurements," *Computational Materials Science*, vol. 37, no. 3, pp. 269-277, 2006.
- [20] A. Kermanpur, M. Shamanian, and V. E. Yeganeh, "Three-dimensional thermal simulation and experimental investigation of GTAW circumferentially butt-welded Incoloy 800 pipes," *Journal of Materials Processing Technology*, vol. 199, no. 1-3, pp. 295-303, 2008.
- [21] S. Kiyoshima, D. Deng, K. Ogawa, N. Yanagida, and K. Saito, "Influences of heat source model on welding residual stress and distortion in a multi-pass J-groove joint," *Computational Materials Science*, vol. 46, no. 4, pp. 987-995, 2009.
- [22] M. Mokhtarishirazabad, M. McMillan, V. D. Vijayanand, C. Simpson, D. Agius, C. Truman, D. Knowles, and M. Mostafavi, "Predicting residual stress in a 316L electron beam weld joint incorporating plastic properties derived from a crystal plasticity finite element model," *International Journal of Pressure Vessels and Piping*, vol. 201, pp. 104868, 2023.
- [23] A. Siyavoshi, S. Shakheshi, M. R. Afshar, M. Hashemzadeh, and M. Noghabi, "Evaluation of welding-induced residual stress and distortion in A-TIG welding of duplex stainless steel," *Journal of Mechanical Engineering and Sciences*, vol. 17, no. 1, pp. 9324-9337, 2023.
- [24] W.-L. Lu, J.-L. Sun, H. Su, L.-J. Chen, and Y.-Z. Zhou, "Experimental research and numerical analysis of welding residual stress of butt welded joint of thick steel plate," *Case Studies in Construction Materials*, vol. 18, pp. e01991, 2023.
- [25] Z. Gao, L. Zhao, and Y. Han, "Investigation on residual stress in SA508/Inconel Metal/CF8A dissimilar welded joint for nuclear steam generator safe end using different processes," *Nuclear Technology*, pp. 1-15, 2023.
- [26] A. K. Abdul Jawwad and M. Mahdi, "Effects of non-symmetric non-uniformly distributed welding residual stress on fatigue failure initiation and propagation in a hydropower generator shaft," *Multidiscipline Modeling in Materials and Structures*, vol. 19, no. 5, pp. 924-952, 2023.
- [27] F. Hosseinzadeh, B. Tafazzoli-Moghaddam, H. K. Kim, P. J. Bouchard, V. Akrivos, A. N. Vasileiou, and M. Smith, "Residual stresses in austenitic thin-walled pipe girth welds: Manufacture and measurements," *International Journal of Pressure Vessels and Piping*, vol. 206, pp. 105016, 2023.
- [28] P. Asadi, S. Alimohammadi, O. Kohantorabi, A. Fazli, and M. Akbari, "Effects of material type, preheating and weld pass number on residual stress of welded steel pipes by multi-pass TIG welding (C-Mn, SUS304, SUS316)," *Thermal Science and Engineering Progress*, vol. 16, pp. 100462, 2020.
- [29] P. Asadi, S. Alimohammadi, O. Kohantorabi, A. Soleymani, and A. Fazli, "Numerical investigation on the effect of welding speed and heat input on the residual stress of multi-pass TIG welded stainless steel pipe," *Proceedings of the Institution of Mechanical Engineers, Part B: Journal of Engineering Manufacture*, vol. 235, no. 6-7, pp. 1007-1021, 2020.
- [30] Y. Liu, P. Wang, H. Fang, and N. Ma, "Mitigation of residual stress and deformation induced by TIG welding in thin-walled pipes through external constraint," *Journal of Materials Research and Technology*, vol. 15, pp. 4636-4651, 2021.
- [31] D. Deng and S. Kiyoshima, "Numerical simulation of residual stresses induced by laser beam welding in a SUS316 stainless steel pipe with considering initial residual stress influences," *Nuclear Engineering and Design*, vol. 240, no. 4, pp. 688-696, 2010.
- [32] A. F. M. Arif, A. S. Al-Omari, B. S. Yilbas, and Y. N. Al-Nassar, "Thermal stress analysis of spiral laser-welded tube," *Journal of Materials Processing Technology*, vol. 211, no. 4, pp. 675-687, 2011.
- [33] J. Xu, J. Chen, Y. Duan, C. Yu, J. Chen, and H. Lu, "Comparison of residual stress induced by TIG and LBW in girth weld of AISI 304 stainless steel pipes," *Journal of Materials Processing Technology*, vol. 248, pp. 178-184, 2017.
- [34] R. Kumar, M. M. Mahapatra, A. K. Pradhan, A. Giri, and C. Pandey, "Experimental and numerical study on the distribution of temperature field and residual stress in a multi-pass welded tube joint of Inconel 617 alloy," *International Journal of Pressure Vessels and Piping*, vol. 206, pp. 105034, 2023.
- [35] F. Kong, J. Ma, and R. Kovacevic, "Numerical and experimental study of thermally induced residual stress in the

- hybrid laser-GMA welding process,” *Journal of Materials Processing Technology*, vol. 211, no. 6, pp. 1102-1111, 2011.
- [36] A. R. Pavan, B. Arivazhagan, M. Zubairuddin, S. Mahadevan, and M. Vasudevan, “Thermomechanical analysis of A-TIG and MP-TIG welding of 2.25Cr-1Mo steel considering phase transformation,” *Journal of Materials Engineering and Performance*, vol. 28, no. 8, pp. 4903-4917, 2019.
- [37] M. Wang, K. Guo, Y. Wei, C. Cao, and Z. Tong, “Welding process optimization for the inner tank of the electric water heater by numerical simulation and experimental study,” *Journal of Manufacturing Processes*, vol. 85, pp. 52-68, 2023.
- [38] S. Bhardwaj, S. K. Aas, and R. M. C. Ratnayake, “Experimental and numerical investigation of residual stresses in proximity girth welds,” *The International Journal of Advanced Manufacturing Technology*, vol. 126, no. 3, pp. 1247-1259, 2023.
- [39] M. Wang, K. Guo, Y. Wei, J. Chen, C. Cao, and Z. Tong, “Failure analysis of cracking in the thin-walled pressure vessel of electric water heater,” *Engineering Failure Analysis*, vol. 143, pp. 106913, 2023.
- [40] N. Moslemi, B. Abdi, S. Gohari, I. Sudin, N. Redzuan, A. Ayob, M. Ahmed, S. Rhee, and C. Burvill, “Influence of welding sequences on induced residual stress and distortion in pipes,” *Construction and Building Materials*, vol. 342, pp. 127995, 2022.
- [41] S.-J. Kim, E.-K. Park, H.-Y. Bae, J.-H. Kim, N.-S. Huh, and Y.-J. Kim, “Finite element welding residual stress analysis of CRDM penetration nozzles,” *Journal of Pressure Vessel Technology*, vol. 144, no. 1, 2021.
- [42] Z. Gao, B. Han, L. Li, G. Ma, and S. Niu, “Numerical simulation of residual stress in post internal-welding process of bimetal composite pipe and optimization of welding sequence,” *International Journal of Pressure Vessels and Piping*, vol. 199, pp. 104730, 2022.
- [43] A. Yaghi, T. H. Hyde, A. A. Becker, W. Sun, and J. A. Williams, “Residual stress simulation in thin and thick-walled stainless steel pipe welds including pipe diameter effects,” *International Journal of Pressure Vessels and Piping*, vol. 83, no. 11-12, pp. 864-874, 2006.
- [44] D. Deng and S. Kiyoshima, “FEM prediction of welding residual stresses in a SUS304 girth-welded pipe with emphasis on stress distribution near weld start/end location,” *Computational Materials Science*, vol. 50, no. 2, pp. 612-621, 2010.
- [45] C. Liu, J. X. Zhang, and C. B. Xue, “Numerical investigation on residual stress distribution and evolution during multipass narrow gap welding of thick-walled stainless steel pipes,” *Fusion Engineering and Design*, vol. 86, no. 4-5, pp. 288-295, 2011.
- [46] IGCAR, *Material Properties for Design*, IGCAR Data Book, 1999.
- [47] M. Ragavendran, M. Vasudevan, and M. Menaka, “Finite element modeling of hybrid laser-TIG welding of type 316L(N) stainless steel,” in *Advances in Computational Methods in Manufacturing, Lecture Notes on Multidisciplinary Industrial Engineering*, R. G. Narayanan et al., Eds. Singapore: Springer Nature Singapore Pte Ltd. 2019, 2019, pp. 259-269.
- [48] B. Taljat, B. Radhakrishnan, and T. Zacharia, “Numerical analysis of GTA welding process with emphasis on post-solidification phase transformation effects on residual stresses,” *Materials Science and Engineering: A*, vol. 246, no. 1-2, pp. 45-54, 1998.
- [49] Y. Javadi, M. Akhlaghi, and M. A. Najafabadi, “Nondestructive evaluation of welding residual stresses in austenitic stainless steel plates,” *Research in Nondestructive Evaluation*, vol. 25, no. 1, pp. 30-43, 2014.
- [50] D. Deng, H. Murakawa, and W. Liang, “Numerical and experimental investigations on welding residual stress in multi-pass butt-welded austenitic stainless steel pipe,” *Computational Materials Science*, vol. 42, no. 2, pp. 234-244, 2008.
- [51] J. Goldak, A. Chakravarti, and M. Bibby, “A new finite element model for welding heat sources,” *Metallurgical Transactions B*, vol. 15, no. 2, pp. 299-305, 1984.
- [52] K. C. Ganesh, M. Vasudevan, K. R. Balasubramanian, N. Chandrasekhar, and P. Vasantharaja, “Thermo-mechanical analysis of TIG welding of AISI 316LN stainless steel,” *Materials and Manufacturing Processes*, vol. 29, no. 8, pp. 903-909, 2014.
- [53] K. C. Ganesh, K. R. Balasubramanian, M. Vasudevan, P. Vasantharaja, and N. Chandrasekhar, “Effect of multipass TIG and activated TIG welding process on the thermo-mechanical behavior of 316LN stainless steel weld joints,” *Metallurgical and Materials Transactions B: Process Metallurgy and Materials Processing Science*, vol. 47, no. 2, pp. 1347-1362, 2016.
- [54] J. Rahman Chukkan, M. Vasudevan, S. Muthukumar, R. Ravi Kumar, and N. Chandrasekhar, “Simulation of laser butt welding of AISI 316L stainless steel sheet using various heat sources and experimental validation,”

Journal of Materials Processing Technology, vol. 219, pp. 48-59, 2015.

- [55] M. S. Sumanlal, N. S. Sivasubramaniyan, V. M. Joy Varghese, M. Shafeek, and D. T. Ananthan, "Estimation of heat source model parameters for partial penetration of TIG welding using numerical optimization method," *Welding International*, vol. 37, no. 7, pp. 400-416, 2023.
- [56] M. Ragavendran and M. Vasudevan, "Laser and hybrid laser welding of type 316L(N) austenitic stainless steel plates," *Materials and Manufacturing Processes*, vol. 35, no. 8, pp. 922-934, 2020.
- [57] M. Ragavendran, M. Vasudevan, and N. Hussain, "Study of the microstructure, mechanical properties, residual stresses, and distortion in type 316LN stainless steel medium thickness plate weld joints," *Journal of Materials Engineering and Performance*, vol. 31, no. 6, pp. 5013-5025, 2022.
- [58] M. Ragavendran, J. G. Kumar, and M. Vasudevan, "Evaluation of tensile properties using uni-axial and ball indentation testing and correlation with microstructure variations across the 316LN stainless steel weld joints," *Materials Science and Engineering: A*, vol. 832, pp. 142445, 2022.
- [59] G. Y. Zhang, W. H. Li, G. J. Xu, F. Xing, L. L. Chang, S. K. Wu, H. B. Liao, and X. Y. Wang, "Simulation of temperature field and residual stress in high-power laser self-melting welding process of CLF-1 steel medium-thick plate," *Fusion Engineering and Design*, vol. 195, pp. 113936, 2023.
- [60] M. Ragavendran and M. Vasudevan, "Effect of laser and hybrid laser welding processes on the residual stresses and distortion in AISI type 316L(N) stainless steel weld joints," *Metallurgical and Materials Transactions B: Process Metallurgy and Materials Processing Science*, vol. 52, no. 4, pp. 2582-2603, 2021.
- [61] N. Hempel, T. Nitschke-Pagel, and K. Dilger, "Residual stresses in multi-pass butt-welded ferritic-pearlitic steel pipes," *Welding in the World*, vol. 59, no. 4, pp. 555-563, 2015.